Hindawi
Structural Control and Health Monitoring
Volume 2023, Article ID 8645831, 24 pages
https://doi.org/10.1155/2023/8645831

Research Article

Mitigation of In-Plane Vibrations in Large-Scale Wind Turbine Blades with a Track Tuned Mass Damper

Wanrun Li,[1,2,3] **Shuanbao Yan**,[1] **Ganggang Li**,[1] **and Yongfeng Du**[1,2,3]

[1]*Institution of Earthquake Protection and Disaster Mitigation, Lanzhou University of Technology, Lanzhou 730050, China*
[2]*International Research Base on Seismic Mitigation and Isolation of GANSU Province, Lanzhou University of Technology, Lanzhou 730050, China*
[3]*Disaster Prevention and Mitigation Engineering Research Center of Western Civil Engineering, Lanzhou University of Technology, Lanzhou 730050, China*

Correspondence should be addressed to Wanrun Li; ce_wrli@lut.edu.cn

Received 25 December 2022; Revised 9 May 2023; Accepted 27 November 2023; Published 18 December 2023

Academic Editor: Zili Zhang

To mitigate in-plane vibrations of wind turbine blades, a track tuned mass damper (TMD) is proposed and its performance for mitigating blade in-plane vibration is investigated considering various influence factors. Firstly, the organization and operational principles of the damping control device are explained. Then, the equations of motion of the individual TMD-equipped blade are then deduced from Euler–Lagrange. Secondly, blade's wind loading is calculated by blade element momentum theory considering the blade rotation effect through the rotating sample spectrum. Thirdly, the dynamical response of the blade based on the MATLAB/SIMULINK tool is calculated. The peak maximum displacement and standard deviation of the blade tip are chosen as the estimation indicators to assess the TMD's effectiveness of the device considering actually various argument including mass ratio μ, damping ratio ξ, and installation position x_0/L. Based on the assumption that the mass block in the vibration reduction control device has no contact with the inside surface of the blade web in operation, the optimal relative values of mass ratio, damping ratio, and installation position of a single blade are determined as 0.03, 15%, and 0.55, respectively. As a result, the reduction of the peak value and the standard deviation can reach 52.78% and 53.75%, respectively. Therefore, with the optimal parameters, the designed vibration control device effectively not only reduces the blade tip displacement but also avoids the damage due to in-plane vibrations.

1. Introduction

Energy is a necessity to drive the sustainable development of the global society [1] and economy. Among many regenerative energy resources, wind power has become a regenerative energy resource that can greatly reduce carbon emissions [2] and fossil fuel consumption due to its unique advantages. Wind energy is harvested by wind turbines to generate electricity. Meanwhile, the industry's net electricity generation has steadily increased. Based on the most recent data provided by GWEC, China's installation capacity for wind output has been in the forefront of the world by 2022. To harvest more energy and cut energy costs, many contemporary multimegawatt wind turbines are engineered with progressively bigger blades [3], rotors, and towers [4]. The larger blade produces serious vibration under wind loading, which degrades the lifetime of the wind turbine and induces blade fatigue.

Under some extreme conditions, a catastrophic complete collapse of the wind turbine can occur. Under external wind loading and blade gravity, the vibration modes within the blades are categorised as flap-wise (the out-of-plane vibration), edgewise (the in-plane vibration) modes, and torsion. Flap-wise vibrations are effectively dampened

aerodynamically during regular operational [5] state, rendering the vibration to be quasistatic [6]. In contrast, in-plane vibrations associated with low aerodynamic [7] and structural damping will lead to increased blade damage. As shown in Figure 1, due to the special structure form of larger wind turbine blades, the combination of damping caused by the structure and damping caused by aerodynamics in the direction of in-plane vibrations is far less than that in the direction of flap-wise [8], which easily leads to the blade's destruction caused by in-plane vibrations. The in-plane vibrations will affect the power output [9] of turbines and the potential catastrophic blade failure, which have also been experimentally demonstrated. Hence, in-plane vibrations have become a particularly significant consideration [10] for wind turbine blades to avoid fatigue damage.

Because of its significance, many scholars at home and abroad began to pay attention to the vibration control of blades from various angles. The current research studies are mainly carried out from three aspects: improving the traditional pitch control strategy, designing a reasonable vibration control device, and changing the skin material of blades. For the vibration damping designs of blades, the variable pitch control system, with the function of maintaining the stable and safe operation of blades, is the most mature one in the development process of the wind turbine. The variable pitch control system reduces blade vibration [11] under different wind speeds by altering the pitch angle of blades and the angle of attack of wind loading on the blades, thereby maintaining a stable blade root torque and capacity power [12]. The blade can be safely protected by loss of wind energy utilization efficiency under high wind speed. Recently, several endeavours focused on the variable pitch control system. A groundbreaking pitch control scheme has been introduced for a wind turbine to decrease the blade root load during variable speed operation [13]. As the constant increase of impeller diameter, an autonomous pitch control approach has been devised to enhance the quality of power generation and prolong the life of wind turbines [14] under unbalanced load. However, due to the limitation of practical technologies and theory, the vibration mitigation performance of variable pitch control systems for blade vibration is limited. Bossanyi [15] pointed out that the variable pitch control system can only reduce part of the torque of the blade root in small blades. However, the inertia torque at the blade root under dynamic excitation increases due to the longer blade, which increases the braking force required by the pitch control system, a braking delay, and a weakening effect. With the growth of larger wind turbines, researchers focus more on mitigating wind turbine blade vibration by various methodologies. Among these, intelligent damping materials are gradually applied in the vibration reduction control of buildings [16], machinery [17], and other industries because of a series of advantages, such as self-adaptiveness, fast response, and self-judgment. Nevertheless, intelligent damping materials cannot fully meet the requirements of aerodynamic performance optimization and lightweight and high strength materials. By adding damping devices to increase the damping energy consumption of the structure itself, the vibrating power from

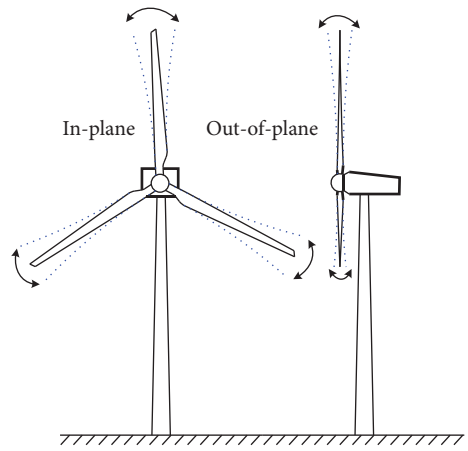

Figure 1: The blade vibration model.

structure is dissipated by the supplemental damping control devices. Much research has been carried out into active, semiactive, and passive control devices for mitigating the blade in-plane vibrations. Although the relevant numerical research has achieved good results, the high price and power demands limit the widespread installation of active as well as semiactive systems in wind turbine blades. In general, a tuned mass damper (TMD) holds an advantage over active and semiactive systems, and in that, it requires no external energy input, which is widely applied in the high-rise building [18] as well as long-span structures, such as Sydney TV Tower in Australia and John Hancock Building in the United States [19]. The vibration reduction rate of TMD in wind-induced structural engineering can reach about 50%. With the diversification of TMD forms [20, 21] and the further promotion of application scope, many scholars are committed to applying TMD to hollow structures such as blades, nacelles, and towers. Fitzgerald et al. [22] firstly proposed to apply TMD to blade vibration reduction. The analysis shows that the reduction rate of blade tip displacement could reach about 39%. Later, an active TMD damping control system linked to the inner wall we at the blade tip by flexible cable [23] was proved to effectively reduce displacement from the blade's tip. Nevertheless, the narrow blade's tip space of the wind turbine cannot effectively meet the displacement required for TMD. Cong and Murtagh et al. [24, 25] put forward the installation of multiple TMDs in wind turbines, which solve the problem of limited TMD space in the web of blades. Dinh and Basu [26] used TMD to conduct in-depth investigation on passive vibration suppression of wind turbine tower. He simplified the wind turbine to a mass series model with multiple degrees of freedom and added TMD at the appropriate position of the model to indirectly lessen the irrational amplitude of blades by adjusting the overall motion displacement of the wind turbine. To better reduce the in-plane vibrations of blades, Zhang et al. successively proposed a cylindrical TLD [27], CLCD [28], and a box TLD [29] to suppress the in-plane vibration of blade in real time. The research shows that these devices can effectively reduce the dynamic vibration of blades in the in-plane direction. Later, Zhang and Larsen

proposed the mathematical expressions for attaining the best calibration (tuning) of the rotational inertia double-tuned mass damper (RIDTMD) [30] to suppress in-plane vibrations within a wind turbine blade in action and compared them with the optimized RIDTMD and optimal TMD. The analysis revealed a greater capability of the RIDTMD to dampen blade vibrations compared to the TMD. Different vibration reduction methods achieve different vibration reduction effects. Qiao et al. [31] performed numerical analysis of the model using the finite element method and proposed an active vibration system to efficiently suppress the vibration of smart blades by obtaining the displacement responds from piezoelectric actuation and piezoelectric sensors. Bolat and Sivrioglu [32] introduced a new active damping structure with magnetorheological layer patch, and the results indicated that the scheme was effective in mitigating vibrations of a small-scale blade. Sivrioglu et al. [33] pointed that mixed norm robust controllers attached to blade structure can successfully attenuate the vibrations of the blade. Staino et al. [34] proposed the double control system of an active cable connection system and pitch control system. When the participation ratio of the double control system is 0.6 and 0.4, respectively, the damping rate in the blade tip displacement is capable of reaching 63%, and the power loss can only reach about 15%. Cong [35] designed a spatial $\mathbf{H}_{\infty}$ controller and a pair of active cables installed at each blade tip to reduce the vibration amplitude. Jokar et al. [36] proposed an actuator configuration which can generate out-of-plane and in-plane bound control loads and introduced a new perturbation observer to assess bounds perturbations for decreasing the HAWT blade vibration. Chen et al. [37] reduced the blade tip displacement-caused torsional vibration by setting a rotating eddy current device inside the blades to achieve energy dissipation.

In the past few years, there has been growing research focus on the vibration damping of blades, focusing on the effect of passive control devices in proposed control strategies. However, there are relatively few studies on the parameters of passive control strategies, especially the investigations regarding the optimization of the parameters in the control strategies. On the contrary, the main tendency for in-plane vibrations control is the design of an active damping control device and the application research of new intelligent material. However, no matter how simple and effective the active device is, its defects, i.e., needing constant external energy, are inevitable. Considering the wind turbine blades in a rotating state for a long time, it is relatively difficult to design the external energy supply. In the area of vibration damping technology, the emergence of new intelligent materials greatly enriches the vibration reduction methods, but there are relatively few intelligent materials to meet the requirements of wind turbine blades' aerodynamic performance optimization, lightweight as well as high strength.

In view of the above problems, this study proposes and investigates a new tuned mass damper for in-plane vibration mitigation of blades. The structure of this paper is as follows: Section 2 explains the composition, model connection, theoretical analysis model, and working principle of the damping control device. Section 3 selects a single blade of a 3-blade horizontal-axis wind turbine as the object of study and simplifies it to a generalized single-degree-of-freedom system, involving just one bending deformation in the in-plane direction. Coupled with Hamilton's principle, the Euler–Lagrange models of motion blades in uncontrolled and controlled states are derived to solve the motion equation of the wind turbine blades under external excitation. Taking into account the effect of rotation affecting the wind velocity, the numerical investigations of the mean wind velocity and the fluctuating wind velocity of the rotating blade are conducted in Section 4, where the wind velocity at each sampling point on the blade. In Section 5, generalized nonconventional powers applied to a solitary blade, concerning the assumed degrees of freedom, primarily consisting of components related to wind loading, gravity, and damping force. The damping in the direction of the assumed degrees of freedom tends to be relatively small, so the damping force is not considered. The wind loading and gravity are mainly calculated for the rotating blade. Section 6 analyzes the influence law of the mass ratio, damping ratio, and installation position of the device on the vibration damping efficiency of the displacement at the blade tip. The vibration mitigation performance designed by the optimal parameters is also analyzed. Lastly, Section 7 sums up the key results of this paper.

2. Configuration of Proposed TMD

Currently, a broad spectrum of vibration control mechanisms is used in building structures [38], bridges [39], and marine engineering [40]. TMD is frequently used as vibration damping devices in the area of vibration. Its working principle is as follows: the structure drives the TMD system to move under external excitation, and the inertia power generated by the TMD system acts on the structure in response to reduce the vibration amplitude of the structure, so as to fulfil the aim of mitigating. A novel tuned mass damping control device, installed in the available space within the blade, is proposed in this paper for mitigating in-plane vibrations. The proposed device is directly installed in the looped frame constituted of the inner web and the main beam of the blade. On the premise of not affecting the aerodynamic characteristics of the blade, the vibration reduction control is investigated. The configurations of the proposed device are shown in Figure 2. It is mainly composed of eight sets of spring systems, four sets of track systems, and a mass block. The sleeve is installed on the mass block which is installed on the track system by the sliding shaft passing through the sleeve. The spring passes through the sliding shaft. Both ends of the spring are, respectively, installed on the inner wall of the web as well as the sleeve through the fixing ring, so as to facilitate the connection of various components and prevent the collision between the mass block as well as the inside of the web. The mass block is contacted with the blade web inner wall by sleeve and spring. When the spring connected the fixed ring and the mass block at the appropriate position is in the minimum compression state, it

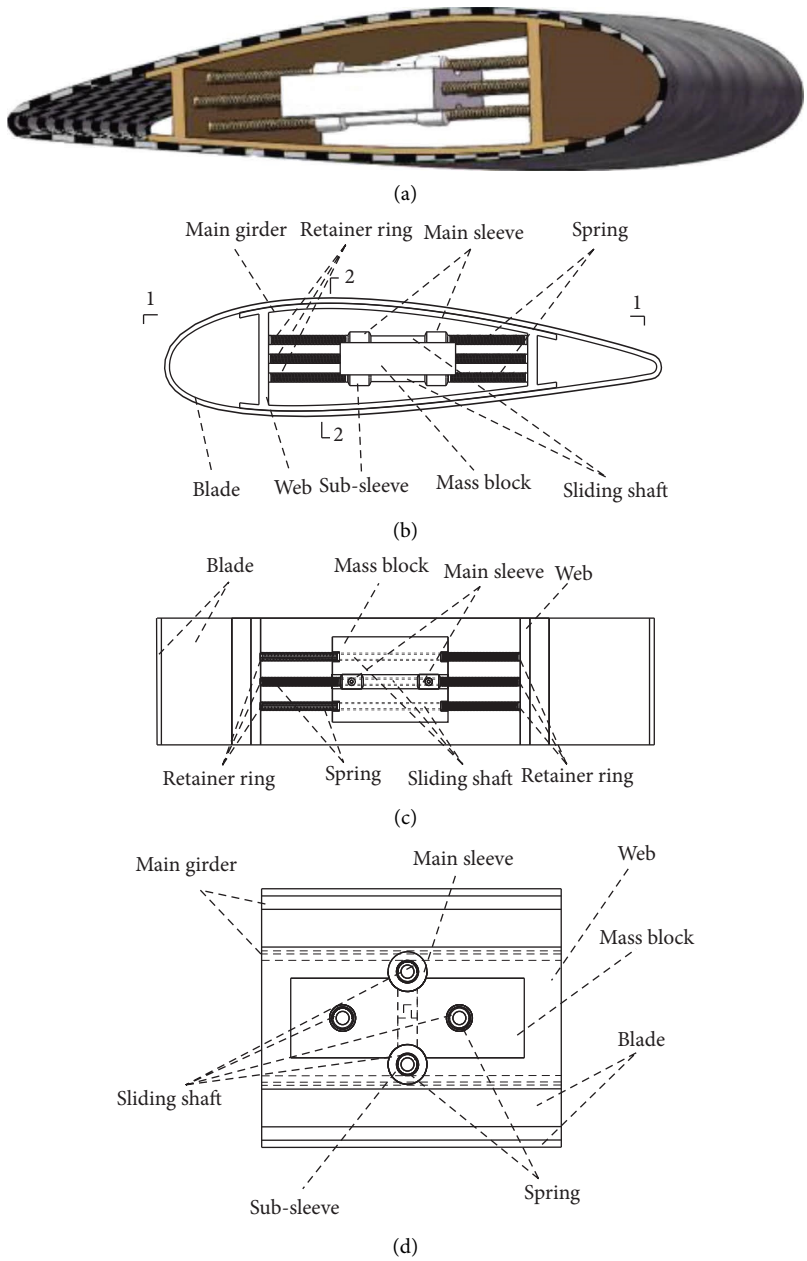

Figure 2: Schematic diagram of vibration reduction control device. (a) Three-dimensional sketch of the device. (b) Elevation view of the device. (c) Section view of device 1-1. (d) Section drawing of device 2-2.

is realistic to fully utilize the space in the wind turbine during the operation of the mass block. Because of its simple structure form, the device is convenient in site construction and can reduce the blade vibration effectively under reasonable design. The damping system designed separately without occupying the space of the track system is conducive to the best performance of the mass block. The mass block has a small volume and occupies a small amount of internal space of the blade during operation, which has a relatively small additional influence on the aerodynamic performance of the blade.

3. Theoretical Model of Proposed TMD

In order to strictly guarantee that the mass block has no contact with the inside surface of the blade web while in action, the damping device needs to be installed in the appropriate place at the blade. As shown in Figure 3, the global coordinate system (X_T, Y_T) is created in the appropriate position of the airfoil where the damping control device is located, in which X_T axis is along the chord direction of the blade element, and Y_T axis is along the vertical center line of the mass block in the static state.

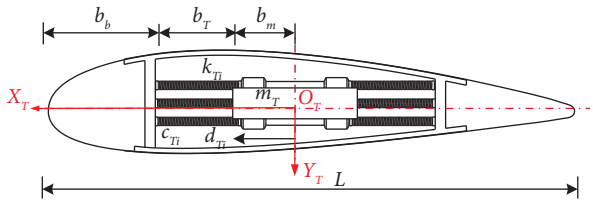

Figure 3: Parameter sketch of damping control device.

In Figure 3, b_T is defined as the effective chord length of the airfoil in which the vibration control device is positioned, taking a quarter of the actual chord length L. d_{Ti} represents the displacement of the mass block of the vibration control device during operation. $m_T = \mu M$ is the mass of the mass block. $c_{\mathrm{Ti}} = 2\xi_T f_T \omega m_T$ is the designed damping. $k_{\mathrm{Ti}} = f_T \omega_T^2 m_T$ is the designed stiffness. Here, μ is the mass ratio between the mass of the mass block and blade modal mass in the vibration damping system. ξ is the damping ratio of the vibration control device. f_T is the frequency ratio of both the frequency of the vibration damping system and the blade modal frequency.

The National Renewable Energy Laboratory (NREL) 5 MW baseline wind turbine is chosen to be the prototype to simulate in-plane responses of the blade. The proposed model and control schemes were simulated in MATLAB (The MathWorks Inc, MA, USA). The specific details of the wind turbine are displayed in Table 1.

Table 1: Specific parameters of NREL-5 MW wind turbine.

Physical parameters	Specific value
Maximum rated power	5 MW
Number of blades	3
Blade diameter length	61.5 m
Height of the hub	90 m
Cut-in/rating/cut-out velocity	3 m/s, 11.4 m/s, 25 m/s
Cut-in/rated velocity	6.9 r/min, 12.1 r/min
Blade Mass	17740 kg
Damping ratio of blade structure	0.48%
Hub diameter	3 m
Tower height	87.6 m
First-order frequency of the blade	1.0606 Hz

The blade is simplified as a cantilever beam mounted on the hub, and the deflection and slope of the modal shape at the hub are zero. According to the literature [22], the modal shape function of the blade is

$$\begin{cases} \phi_{\mathrm{in}}(x) = -0.6893x^6 + 2.3738x^5 - 3.6043x^4 + 2.5737x^3 + 0.3461x^2, \\ \phi_{\mathrm{out}}(x) = -2.4766x^6 + 5.1976x^5 - 3.4820x^4 + 1.7085x^3 + 0.00525x^2, \end{cases} \tag{1}$$

where $x = r/\mathrm{L}$, r is the blade's length across the radial distance from the hub. The modal shape is shown in Figure 4.

An Euler–Lagrangian wind turbine computational model, which relies on an energy equation, has been created, taking into account the structural dynamics of the device and the relationship between in-plane and out-of-plane blade vibration. The wind turbines are complex power production systems, and the blades are in a state of rotation under wind, which is different from building structures in the civil engineering industry. In this study, the blade in a 3-blade horizontal-axis wind turbine condensed as an Euler–Bernoulli beam, is considered as a cantilever shell structure installed on the hub. The blade is considered to be a generalized system with a single degree of freedom and only has a solitary flexural deformation along the in-plane direction. After the hub rotates around the center point, the Euler–Lagrange motion model derived from Hamilton's principle is applied to solve the equations of motion under external action. The equation of motion, in which the Euler–Lagrange formula is a generalized energy equation, indirectly reflects the possible coupling relationship between the various degrees of freedom, that is,

$$\frac{\mathrm{d}}{\mathrm{d}t}\left(\frac{\partial T}{\partial \dot{q}_i}\right) - \frac{\partial T}{\partial q_i} + \frac{\partial V}{\partial q_i} = Q_i. \tag{2}$$

Here, T represents the kinematic energy of the frame, V represents the potential energy, q_i represents the generalized coordination, and Q_i represents generalized force at the ith degree of the freedom system.

To effectively differentiate the different states of blades before and after using the TMD vibration reduction control device. The situation of the wind turbine without the TMD vibration reduction device is characterized as the out-of-control case, and the wind turbine with the TMD vibration reduction control device is defined as the controlled case. The dynamic models of blades are derived separately for uncontrolled and controlled scenarios.

3.1. Derivation of Blade Dynamic Model without Control. Generally, the typically generalized coordinates are selected in the system to facilitate the calculation of the reference point displacement. In this study, because the blade has infinite degrees of freedom, only the in-plane tip displacement of blade is selected as the generalized coordinate for the study. The wind turbine blade would be simplified to a single degree of freedom system for analysis. It is assumed that only a single bending deformation form can be generated. To make the analysis easier, two reference frames are created. One corresponds to the global plane coordinates (X, Y) in the plane, while the second represents the rotational rectangular coordinate (x, y) alongside axis of the blade.

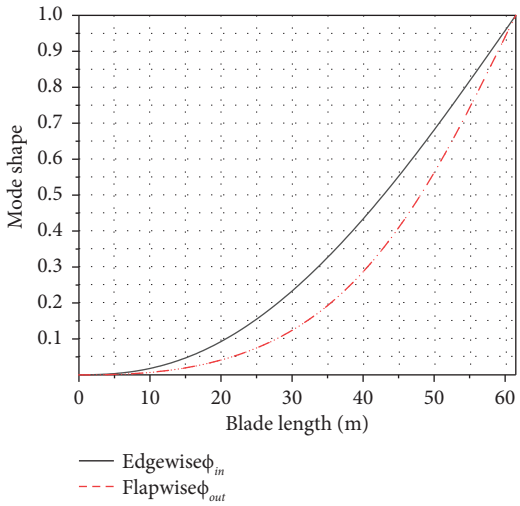

Figure 4: Mode shapes of wind turbine blade.

The initial point for both coordinate reference frame is the hub pivot points, as shown in Figure 5.

To maximize the alignment of the wind turbine with the single-degree-of-freedom system, it is assumed that the deformation of the system only is corresponding to the displacement shape function $\phi_{\text{in}}(x)$. The in-plane blade's movement of radial x is

$$\eta(x,t) = \phi_{\text{in}}(x) q_{i,\text{in}}(t), \tag{3}$$

where $\phi_{\text{in}}(x)$ is the displacement shape function of the first blade deformed along the rotation plane and $q_{i,\text{in}}(t)$ is the generalized coordinate of the in-plane blade's tip.

3.1.1. Potential Energy of Wind Turbine Blade. Following the strain potential energy, $V = (1/2)\text{kx}^2$, where k is composed of the elastic stiffness coefficient as well as the geometric stiffness coefficient, x is the displacement required to generate the strain potential energy. Combined with the generalized displacement definition of blades, the potential energy expression of blades can be obtained as

$$V_{\text{couple}} = \frac{1}{2}\left(k_{e,\text{in}} + k_{g,\text{in}} + k_{\text{gr,in}}\right) q_{i,\text{in}}^2, \tag{4}$$

$k_{e,\text{in}}$ is the in-plane elastic stiffness of the blade. $k_{\text{gr,in}}$ represents the in-plane geometrical stiffness induced by the centripetal force of the blade. $k_{g,\text{in}}$ is the in-plane geometrical stiffness generated by the gravity of the blade. Following the principle of virtual work, if a device is in a state of equilibrium under the influence of an external force, the virtual work of an external force is equal to the virtual deformation work accepted by the deformable body when the system produces a small virtual displacement satisfying the constraint condition. That is, $W_E = W_I$. Then, the stiffness factors of the blade are solved.

Supposing that the unit displacement at blade's tip occurs, that is $\eta(L) = 1$, the inner force moment produced within the entire blade is

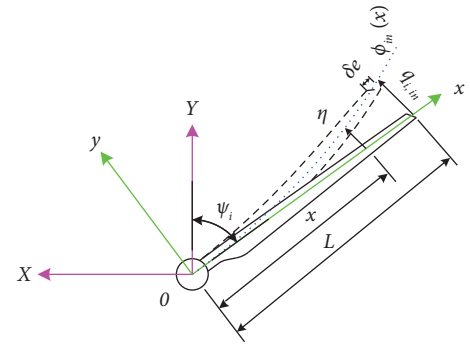

Figure 5: Simplified schematic diagram of wind turbine blade.

$$M(x) = EI_{\text{in}}(x)\phi''_{\text{in}}(x), \tag{5}$$

where EI_{in} represents in-plane bending stiffness of the blade; L is the blade's length. Assuming that the blade tip induces a virtual displacement of $\delta\eta_b$, it can be derived from equation (3) that the virtual displacement produced by the whole wind turbine blade can be described as $\delta\eta(x) = \phi_{\text{in}}(x)\delta\eta_b$.

Combining the correlation of displacement and curvature in materials science, it can be concluded that the virtual curvature generated by hypothetical displacement is

$$\frac{\partial^2[\delta\eta(x)]}{\partial x^2} = \phi''_{\text{in}}(x)\delta\eta_b. \tag{6}$$

Following the principle of the deformable body virtual work, when the virtual displacement at blade tip is $\delta\eta_b$, the virtual work of external force W_I and the virtual strain work W_E obtained by the deformed object are calculated as follows:

$$\begin{aligned} W_I &= \delta\eta_b \int_0^L EI(x)\phi''_{\text{in}}(x)\varphi''_{\text{in}}(x)dx \\ &= \delta\eta_b \int_0^L EI(x)\phi''_{\text{in}}(x)^2 dx, \end{aligned} \tag{7}$$

$$W_E = \delta\eta_b k_{e,\text{in}}. \tag{8}$$

If equations (7) and (8) are equal, the elastic stiffness coefficient in-plane wind turbine blade is $k_{e,\text{in}} = \int_0^L \text{EI}_{\text{in}}(x)\phi''_{\text{in}}(x)^2 \text{d}x$.

Figure 6 demonstrates that the δe shows how the blade shifts axially through elastic deformation caused by vibration. The dx microsection is chosen at any location in the axis direction of the blade. It is assumed that the $d\delta e$ represents the relative displacement induced by the microsection due to outside forces, then

$$\frac{\text{d}\delta e}{\text{d}\delta\eta} = \text{d}\frac{\eta}{\text{d}x} \Longrightarrow \text{d}\delta e = \frac{\text{d}\eta}{\text{d}x}\delta\left(\frac{\text{d}\delta\eta}{\text{d}x}\cdot\text{d}x\right). \tag{9}$$

Following the principle of deformable body virtual work, the virtual work W_I of the external force of blade and the virtual deformation work W_E are given as follows:

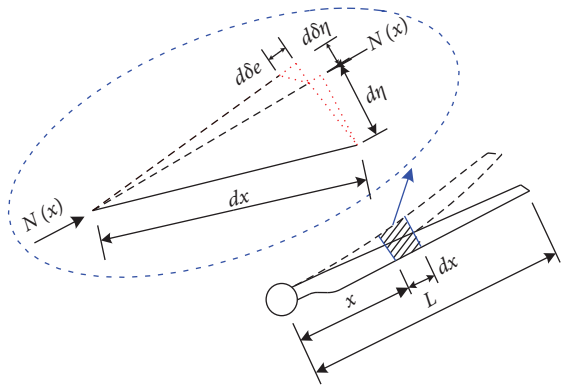

FIGURE 6: Diagram showing the calculation of axial blade's displacement.

$$W_I = \int_0^L N(x)\frac{\mathrm{d}\eta}{\mathrm{d}x}\delta\left(\frac{\mathrm{d}\eta}{\mathrm{d}x}\right)\mathrm{d}x = \delta\eta_{\mathrm{tip}}\int_0^L N(x)\frac{\mathrm{d}\phi_{\mathrm{in}}(x)}{\mathrm{d}x}\frac{\mathrm{d}\phi_{\mathrm{in}}(x)}{\mathrm{d}x}\mathrm{d}x, \tag{10}$$

$$W_E = \delta\eta_{\mathrm{tip}}k_{g,\mathrm{in}}. \tag{11}$$

If equations (10) and (11) are equal, $k_{N,\mathrm{in}} = \int_0^L N(x)\phi'_{\mathrm{in}}(x)^2\mathrm{d}x$ is the coefficient for the geometric stiffness of the blade, in which $N(x)$ is the axial force of the blade.

The axial load on the blade can be split into the centrifugal load outward flow and the gravitational force radial inward flow of the component, as shown in Figure 7. Assuming that the dx is chosen at any location x of the blade for uniform circular motion, $\mathrm{d}F(x) = m(x)\mathrm{d}x\Omega^2 x$ represents the centrifugal power produced by the microsection, in which Ω is the angular velocity of the blade rotation, then the ith blade azimuth can be expressed as $\Psi_i = \Omega t + (2\pi/3)(i-1)$, the entirety of the blade's centrifugal force at position x can be obtained by integrating along L–x, that is, $F(x) = \int_x^L \Omega^2 m(\varsigma)\varsigma d\varsigma$.

$N(x) = G(x) = \int_x^L \mathrm{gm}(\varsigma)\cos\Psi_i d\varsigma$ represents the radial axial force induced by gravity on the blade, where $m(\varsigma)$ is mass per unit of distance in the radial direction of the blade, so the geometrical stiffness is

$$k_{\mathrm{gr,in}} = \int_0^L\int_x^L \Omega^2 m(\varsigma)\varsigma\mathrm{d}\varsigma\phi'_{\mathrm{in}}(x)^2\mathrm{d}x,$$
$$k_{g,\mathrm{in}} = \int_0^L\int_x^L \mathrm{gm}(\varsigma)\cos\Psi_i\mathrm{d}\varsigma\phi'_{\mathrm{in}}(x)^2\mathrm{d}x. \tag{12}$$

Accordingly, the potential energy may be obtained as

$$V = \frac{1}{2}\int_0^L\left[\mathrm{EI}_{\mathrm{in}}(x)\phi''^{\,2}_{\mathrm{in}} + F(x)\phi'^{\,2}_{\mathrm{in}} + G(x)\phi'^{\,2}_{\mathrm{in}}\right]\mathrm{d}x. \tag{13}$$

3.1.2. Kinetic Energy of Wind Turbine Blade. For blades in rotation, the velocity is calculated in the stationary reference frame (x, y), then

$$v_i^2(\mathrm{t}) = \left(-\Omega\phi_{\mathrm{in}}(x)q_{i,\mathrm{in}}\right)^2 + \left(\Omega x + \phi_{\mathrm{in}}(x)\dot{q}_{i,\mathrm{in}}\right)^2. \tag{14}$$

According to the calculation equation of the kinetic energy, the blade's kinetic energy may be obtained as

$$T = \frac{1}{2}\int_0^L m(x)v_i^2(t)\mathrm{d}x = \frac{1}{2}\Omega^2 q_{i,\mathrm{in}}^2\int_0^L m(x)\phi_{\mathrm{in}}{}^2(x)\mathrm{d}x + \frac{1}{2}\Omega^2\int_0^L m(x)x^2\mathrm{d}x + \frac{1}{2}\dot{q}_{i,\mathrm{in}}^2\int_0^L m(x)\phi_{\mathrm{in}}^2(x)\mathrm{d}x + \Omega\dot{q}_{i,\mathrm{in}}\int_0^L m(x)x\phi_{\mathrm{in}}(x)\mathrm{d}x. \tag{15}$$

By inserting equations (13) and (15) into equation (2), the dynamic model of the blade for the uncontrolled case can be obtained as

$$\mathrm{M}\ddot{\mathrm{q}}(t) + \mathrm{C}\dot{\mathrm{q}}(t) + \mathrm{Kq}(t) = Q, \tag{16}$$

where the expressions of each parameter are explained as follows: $M = \int_0^L m(x)\varphi(x)^2\mathrm{d}x$, $C = a_1\int_0^L \mathrm{EI}(x)\varphi''(x)^2\mathrm{d}x$, and $K = \int_0^L \mathrm{EI}(x)\varphi''(x)^2dx - \int_0^L\int_x^L(-\Omega^2 m(\varsigma)\varsigma + \mathrm{gm}(\varsigma)\cos\psi)d\varsigma\phi'(x)\mathrm{d}x$.

Q represents the outside load acting on an individual blade, i.e., $Q = Q_{i,g} + Q_{i,\mathrm{in}}$, where $Q_{i,g}$ is the gravity load along the in-plane direction and $Q_{i,\mathrm{in}}$ is the wind loading along the in-plane direction.

3.2. Derivation of Blade Dynamic Model with Control. The vibration reduction control device, which is simplified as a TMD vibration reduction system with damping and stiffness installed at a particular location on the blade, is installed in the radial direction x_0 of the blade. As shown in Figure 8, the difference between the displacement of the blade at x_0 and the motion displacement of the TMD is $x_{\mathrm{Ti}}(t) = \phi_{\mathrm{in}}(x_0)q_{i,\mathrm{in}} - d_{\mathrm{Ti}}$, where d_{Ti} is the generalized coordinate of the TMD.

Combined with equation (4), the potential energy in the coupled dynamic model of the blade and vibration reduction control device can be obtained as

$$V_{\mathrm{couple}} = \frac{1}{2}\left(k_{e,\mathrm{in}} + k_{\mathrm{g,in}} + k_{\mathrm{gr,in}}\right)q_{i,\mathrm{in}}^2 + \frac{1}{2}k_{\mathrm{Ti}}\left(q_{i,\mathrm{in}}\phi_{\mathrm{in}}(x_0) - d_{\mathrm{Ti}}\right)^2. \tag{17}$$

Considering the effect of blade rotation on the TMD's velocity, the velocity generated by vibration control under external excitations is

$$v_{\mathrm{Ti}}(t) = \left(-\Omega\phi_{\mathrm{in}}(x_0)q_{i,\mathrm{in}} - \Omega\mathrm{d}_{\mathrm{Ti}}\right)^2 + \left(\Omega_{x_0} + \phi_{\mathrm{in}}(x_0)\dot{q}_{i,\mathrm{in}} + \dot{d}_{\mathrm{Ti}}\right)^2, \tag{18}$$

where k_{Ti} is the stiffness of the vibration reduction control device.

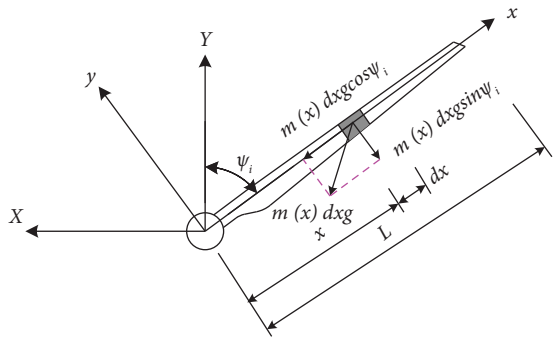

Figure 7: Gravitation decomposition diagram of the blade.

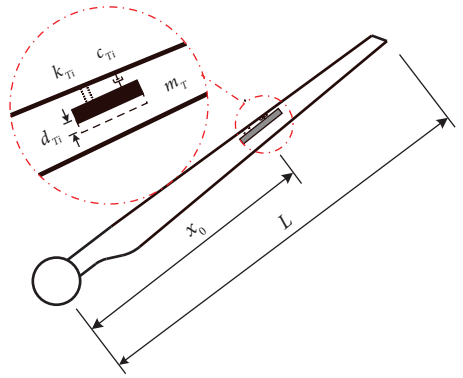

Figure 8: Simplified diagram of the vibration control device.

Combined with equations (15) and (18), the kinetic energy term in the coupled dynamic model of wind turbine blade as well as vibration reduction control device can be obtained as

$$T_{\text{couple}} = \frac{1}{2}\int_0^L m(x)v_i^2\,\mathrm{d}x + \frac{1}{2}m_T\sum_{i=1}^{3}v_{\text{Ti}}^2 = \frac{1}{2}\int_0^L m(x)\begin{pmatrix}\Omega^2\phi_{\text{in}}^2(x)q_{i,\text{in}}^2 + \Omega^2x^2 + \phi_{\text{in}}^2(x)\dot{q}_{i,\text{in}}^2\\ +2\Omega x\phi_{\text{in}}(x)\dot{q}_{i,\text{in}}\end{pmatrix}\mathrm{d}x$$
$$+\frac{1}{2}m_T\begin{pmatrix}\Omega^2\phi_{\text{in}}^2(x_0)q_{i,\text{in}}^2 + \Omega^2\mathrm{d}_{\text{Ti}}^2+2\Omega^2\phi_{\text{in}}(x_0)q_{i,\text{in}}d_{\text{Ti}}\\ +\Omega^2x_0^2 + \phi_{\text{in}}^2(x_0)\dot{q}_{i,\text{in}}^2+2\Omega x_0\phi_{\text{in}}(x_0)\dot{q}_{i,\text{in}}\\ +\dot{\mathrm{d}}_{\text{Ti}}^2+2\Omega x_0\dot{\mathrm{d}}_{\text{Ti}}+2\phi_{\text{in}}(x_0)\dot{q}_{i,\text{in}}\dot{d}_{\text{Ti}}\end{pmatrix}, \tag{19}$$

where m_T stands for the mass of the mass block in the vibration reduction control device.

By substituting equations (16) and (18) into equation (2), the dynamic model of the blade in the controlled situation may be acquired as

$$\begin{cases} \left(\int_0^L m(x)\phi_{\text{in}}^2(x)\mathrm{d}x + m_T\phi_{\text{in}}^2(x_0)\right)\ddot{q}_{i,\text{in}} + m_T\phi_{\text{in}}(x_0)\ddot{d}_{\text{ji}} + c_b\int_0^L \phi_{\text{in}}(x)\mathrm{d}x\dot{q}_{i,\text{in}} \\ -\left(m_T\Omega^2{\phi_{\text{in}}}^2(x_0) + \Omega^2\int_0^L m(x){\phi_{\text{in}}}^2(x)\mathrm{d}x - \left(k_{e,\text{in}} + k_{\text{g,in}} + k_{\text{gr,in}}\right) - k_{\text{Ti}}\phi_{\text{in}}^2(x_0)\right)q_{i,\text{in}} \\ + c_{\text{Ti}}\phi_{\text{in}}(x_0)\dot{q}_{i,\text{in}} - c_{\text{Ti}}\dot{\mathrm{d}}_{\text{Ti}} - \left(m_T\Omega^2 + k_{\text{Ti}}\right)\phi_{\text{in}}(x_0)d_{\text{Ti}} = Q, \\ m_T\ddot{d}_{\text{Ti}} + m_T\phi_{\text{in}}(x_0)\ddot{q}_{i,\text{in}} - c_{\text{Ti}}\phi_{\text{in}}(x_0)\dot{q}_{i,\text{in}} + c_{\text{Ti}}\dot{d}_{\text{Ti}} + \left(k_{\text{Ti}} - m_T\Omega^2\right)d_{\text{Ti}} - \left(m_T\Omega^2 + k_{\text{Ti}}\right)q_{i,\text{in}}\phi_{\text{in}}(x_0) = m_T g\sin(\Omega t) \\ 0 < \mathrm{d}_{\text{Ti}} < b_T = \frac{1}{4}L_T, \end{cases} \tag{20}$$

where b_T is defined as the effective chord length of the airfoil at the place of the vibration control device, taking a quarter of the actual chord length L_T. d_{Ti} represents the displacement of the mass block of the vibration damping system during operation.

4. Wind Field Simulation considering Blade Rotation

The spatial wind field is assumed to be a standardized random field with certain time-varying characteristics. For most large building structures in a static state, the wind speed acting on these buildings only needs to consider the time-varying characteristics of wind velocity at every point and the correlation between spatial points when the spatial position is determined. However, for the rotating blade, the spatial position changes periodically with time. The wind velocity acting on the blade needs to consider the time-varying characteristics of wind velocity at each point and the correlation between spatial points. Meanwhile, it also needs to note the impact of the operation point on the periodic change of the spatial position of the blade rotation [41]. From a functional perspective, this paper focuses on the in-plane vibration damping of the blade in a rotating state. To meet the characteristics of natural wind as much as possible, the influence of the rotation effect of the blades on wind speed is considered. It is supposed that the wind wheel is in a uniform compressible and isotropic turbulent wind field. Generally, the natural wind velocity includes the mean wind speed calculated according to the long-term statistical law and the fluctuating wind speed simulated according to its power spectrum. In this study, four sampling points were selected for each blade while the blade is turning. Each sampling point was selected based on the blade element composition of the blade. The specific distribution is shown in Figure 9.

4.1. Simulation of Mean Wind Speed of Rotating Blades. The mean wind velocity is affected by the ground roughness and the height from the ground. The phenomenon that the wind velocity changes along the height is known as wind shear. At present, there are two kinds of wind shear models: the exponential model and the logarithmic model. According to the IEC Standard as well as the GL Standard, it is pointed out that the exponential model is more suitable for the practical mean wind velocity. Therefore, the exponential model is applied to gain the mean wind velocity of the wind turbine blade in this paper. The reference point is selected as the hub midpoint height of wind turbine.

The model that takes into account the wind shear effect follows an exponential function and is denoted as

$$\overline{U}(z) = \overline{U_h}(z)\cdot\left(\frac{z}{z_h}\right)^{\beta}, \tag{21}$$

where the mean wind speed at heights of $\overline{U}(z)$ and $\overline{U_h}(z_h)$ above the ground z as well as z_h, respectively, and z_h represents the height of the center point of the hub. $z = z_h + r\cos\alpha$ represents the periodically changing height of a certain point on the wind turbine blade.

In this research, if the rated wind speed of the hub is $\overline{U}_h = 12m/s$, the mean wind velocity acting on each point of the blade is displayed in Figure 10. It should be noted that the rated wind velocity adopted here is not 11.4 m/s in Table 1. Because the average wind speed was simulated using the exponential model, according to formula (20), then the rated wind velocity $\overline{U}_h = 12m/s$ at the hub center point was used to simulate the average wind velocity at every sampling point. On the same blade, the mean wind speed of each point is in the same phase, and the peak value of the average wind speed increases with the increase of the blade radius. In the process of blade rotation, the mean wind speed varies periodically.

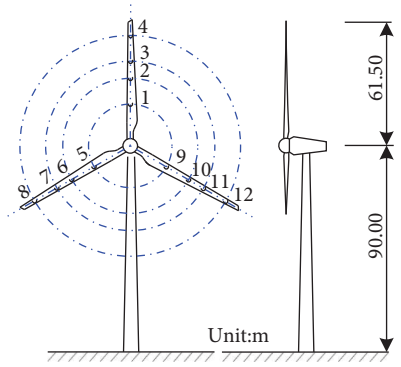

Figure 9: Distribution of sampling points in the rotating plane of wind turbine blade.

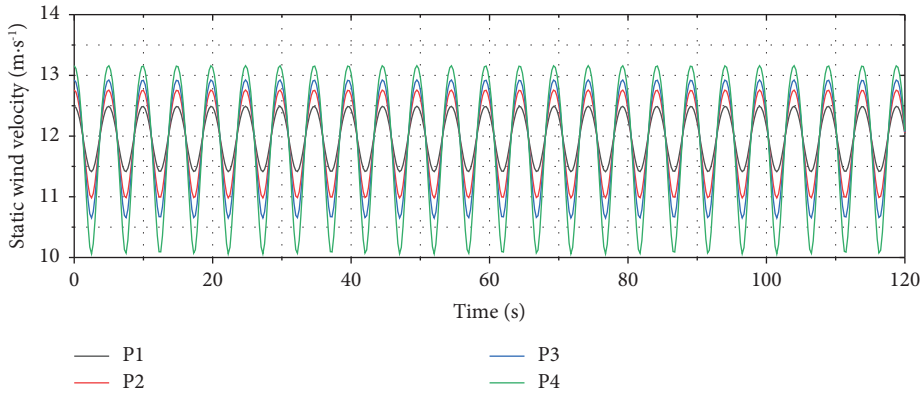

Figure 10: Average blade wind speed at each point.

4.2. Blade Rotation Effect. Because of the influence of air pressure and the ground roughness, the wind velocity fluctuates in the high-frequency part for a short time, which is usually expressed by the fluctuating wind speed. During the blade's rotational operation, when the pulsating wind speed considers the longitudinal wind velocity only, it can be simplified as a stationary ergodic stochastic process related to time as well as space, which is calculated by using its power spectrum. Let the rotation frequency of the blade be f_0. The wind velocity time history sample at moment t in radial r of blade is u_1. The wind velocity time history sample at moment $t + \tau$ be u_2. Taking the Von–Karman spectrum as the source spectrum, the self-spectrum, as well as the cross-spectrum of the rotating sample spectrum considering the effect of wind turbine blade, are, respectively,

$$\begin{cases} S_{uu} = \dfrac{1}{2\pi} \displaystyle\sum_{m=-\infty}^{+\infty} e^{-i\theta(f-mf_0)} S_{uu}(f-mf_0) \int_0^{2\pi} \cos(m\alpha)\gamma(\alpha, f-mf_0)\mathrm{d}\alpha, \\ S_{u_1u_2} = \dfrac{1}{2\pi} \displaystyle\sum_{m=-\infty}^{+\infty} e^{i[m\alpha_0-\theta(f-mf_0)]} S_{uu}(f-mf_0) \int_0^{2\pi} e^{-\mathrm{im}(2\pi f_0\tau+\alpha_0)} \gamma'(\alpha, f-mf_0)\mathrm{d}\alpha, \end{cases} \tag{22}$$

where $\gamma(\tau, f)$, reflecting the change of amplitude spectrum, is a coherent function, and can be obtained using the Davenport exponent form

$$\gamma(\tau, f) = \exp\left(-\frac{\alpha \cdot \mathrm{d}(\tau) \cdot f}{\overline{U}}\right), \tag{23}$$

where α is the attenuation coefficient. According to the IEC Standard, $\alpha = 10$; $\overline{U}$ is the mean wind speed; $d(\tau)$ and $d'(\tau)$ represent the distance between two sampling points, where $d'(\tau) = \sqrt{r_1^2 + r_2^2 - 2r_1r_2\cos(\alpha+\alpha_0)}$, $d(\tau) = 2r|\sin(\alpha/2)|$, and $\alpha = 2\pi f_0\tau$. α_0 is the initial phase, as shown in Figure 11.

If two dots are on the identical blade, $\alpha_0 = 0$. If two dots are on disparate blades, $\alpha_0 = 2\pi/3$. The Von–Karman source spectrum involved is

$$\frac{f \cdot S_{uu}(f)}{\sigma_u^2} = \frac{4fL_u/\overline{U}}{\left(1 + 6fL_u/\overline{U}\right)^{5/3}}. \quad (24)$$

According to IEC, the integral scale of turbulence is $L_u = 8.1\Delta_1$, where Δ_1 is the scale of longitudinal turbulence, and selected as 42 m. The standard deviation of longitudinal turbulence is $\sigma_u = I_{\text{ref}}(0.75\overline{U}_h + 5.6)$, and I_{ref} denotes the expected value of turbulence is 0.16 at a wind velocity of 15 m/s.

The rotating sample spectrum is composed of an infinite number of source spectrum that are translated by an integer multiple of the rotating frequency of the wind turbine blade and then multiplied by the corresponding weighting coefficient. The mth mode, which is the Fourier expansion coefficient of the coherence function, is $1/2\pi \int_0^{2\pi} e^{-\text{im}(2\pi f_0 \tau + \alpha_0)} \gamma'(\alpha, f - \text{mf}_0) d\alpha$ after shifting the weighting coefficient, where $e^{-\theta i(f-\text{mf}_0)}$ is the phase delay caused by rotation effect and $e^{\text{im}\alpha_0}$ is initial phase information. When $\alpha_0 = 0$ and $r_1 \neq r_2$, it represents the cross-spectrum from various dots on the same blade. When $\alpha_0 \neq 0$, it represents the cross-spectrum between various dots on distinct blades. When $\alpha_0 = 0$ and $r_1 = r_2$, it represents the self-spectrum of each point on the same blade. As shown in Figure 12, the mth mode has a peak near the m-octave of the rotation frequency, and the peak value gradually falls as the value of increases. There is a decrease in the m-order mode, which will result in the decrease phenomenon of the rotation sample spectrum at the mth rotation frequency.

Figure 13 describes the relationship between the self-spectrum and cross-spectrum of the rotating sample spectrum between different sampling points on the same blade and the relationship between the cross-spectrum of each point on different blades. On the same blade, the self-spectrum of a sampling point and the cross-spectrum of another sampling point are quite different. In the high-frequency part, the cross-spectrum decreases rapidly and is gradually close to 0. Under the condition of the same radius of different blades, the changing trend of the cross-spectrum between the two sampling points and any one of the self-spectrums is the same but slightly different from that in the high-frequency part, which indicates that the angle between blades has little influence on the cross-spectrum between sampling points of different blades. The variation trend between the self-spectrum Von–Karman and source spectrum in rotating sample spectrum is the same. Due to the influence of the coherence function in the rotating sample spectrum, the peak value of the rotating sample spectrum appears to drop at a high frequency, and the energy distribution of the rotating sample spectrum is at a high frequency relative to the Von–Karman spectrum.

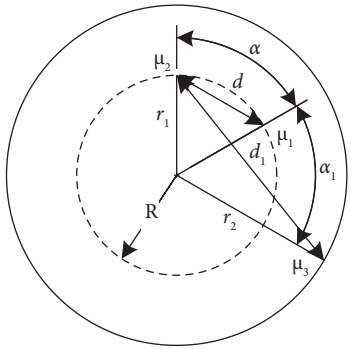

Figure 11: Geometrical relationship of sampling points of the wind turbine blade.

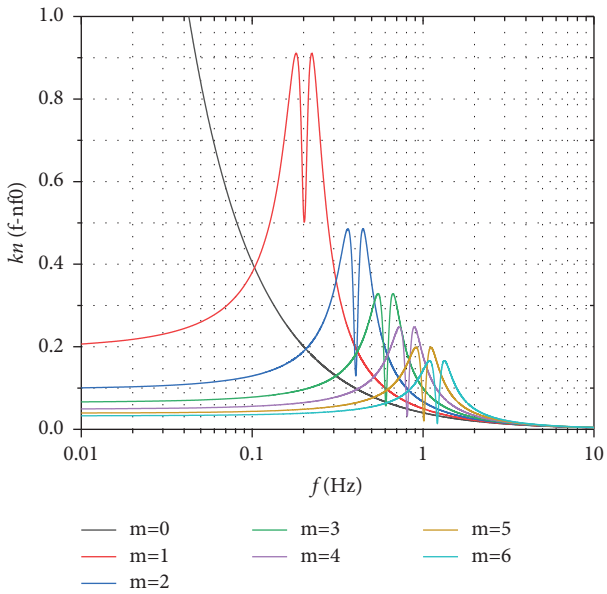

Figure 12: Rotation sample spectrum n-order mode.

4.3. Simulation of Fluctuating Wind Speed of Rotating Blade. The power spectrum mainly describes the statistical characteristics of the energy distribution over frequency in the random process. There is a great difference between the turbulent wind speed spectrum of the fixed point and that of the rotating blade, the energy distribution of which has changed fundamentally. To accurately explore the impact of the rotating effect on the wind load applied on the wind turbine, the rotation sample spectrum is employed to simulate the wind speed of the wind field where the wind turbine is located on the basis of the Von–Karman spectrum. The simulated wind speed is solved by Cholesky decomposition. For the calculation of the fluctuating wind field, the corresponding amplitude spectrum can be obtained by calculating the modes of the self-spectrum and cross-spectrum of each point in the rotating sample spectrum. Therefore, a one-dimensional multivariable

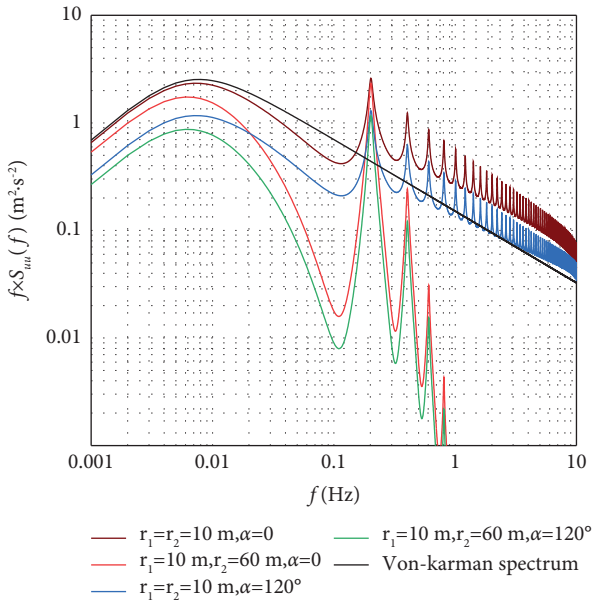

FIGURE 13: The comparison between the rotational spectrum and Von–Karman spectrum.

amplitude-spectrum matrix is constructed from the auto-spectrum and cross-spectrum of the rotating sample spectrum as follows:

$$\overline{S}_{\mathrm{uu}}(f) = \begin{bmatrix} \overline{S}_{u_1u_1}(f) & \overline{S}_{u_1u_2}(f) & \cdots & \overline{S}_{u_1u_n}(f) \\ \overline{S}_{u_2u_1}(f) & \overline{S}_{u_2u_2}(f) & \cdots & \overline{S}_{u_2u_n}(f) \\ \vdots & \vdots & \ddots & \vdots \\ \overline{S}_{u_nu_1}(f) & \overline{S}_{u_nu_2}(f) & \cdots & \overline{S}_{u_nu_n}(f) \end{bmatrix}. \quad (25)$$

The matrix of equation (22) is decomposed by Cholesky factorization, $\overline{S}_{\mathrm{uu}}(f) = \tilde{H}(f)\tilde{H}^T(f)$, where $\tilde{H}(f)$ is the lower triangular matrix.

$$\overline{H}_{\mathrm{uu}}(f) = \begin{bmatrix} \tilde{H}_{u_1u_1}(f) & 0 & \cdots & 0 \\ \tilde{H}_{u_2u_1}(f) & \tilde{H}_{u_2u_2}(f) & \cdots & 0 \\ \vdots & \vdots & \ddots & \vdots \\ \tilde{H}_{u_nu_1}(f) & \tilde{H}_{u_nu_2}(f) & \cdots & \tilde{H}_{u_nu_n}(f) \end{bmatrix}. \quad (26)$$

The harmonic superposition method is a mathematical simulation scheme based on the summation of a series of triangular series and using a discrete spectrum to approximate the target random process. The fluctuating wind velocity applied on the wind turbine blade may be viewed as a process driven by the rotating sample spectrum. According to Shinozuka's theory, the process may be described as

$$\tilde{u}_j(t) = \sum_{p=1}^{j}\sum_{q=1}^{M} 2\sqrt{\pi\Delta f}H_{\mathrm{jp}}\left(f_{\mathrm{pq}}\right)\cos\left(2\pi f_{\mathrm{pq}}t + \alpha_{\mathrm{pq}} - \theta(f)\right), \quad (27)$$

where j is the count of simulation points; M is the frequency division count of fluctuating wind; f_{pq} is the double exponent frequency. $f_{\mathrm{pq}} = q\Delta f - (p/k)\Delta f$, $q = 1, 2, \cdots, M$, $\Delta f = f_u/M$ is the frequency step; f_u is the cut-off frequency, and its value is determined by the area ratio of interval $[0, f_u]$ and interval $[0, \infty]$ in the power spectrum of rotating samples. Generally, the ratio needs to be close to 1, which can be determined according to the criterion of $\int_0^{f_u}|S(f)|\mathrm{d}f = (1-\varepsilon)\int_0^{\infty}|S(f)|\mathrm{d}f$, which ε is far less than 1. In this study, four sampling points were taken on each blade, with $m = 2400$ and $f_u = 10$. According to the sampling theorem, the time steps $\Delta t \le (1/2f_u)$ when the time history sample is generated. $\theta(f) = 2\pi f\tau$ is phase delay parameters. α_{pq} is a random phase angle, which is evenly distributed on the interval $[0, 2\pi]$.

The wind velocity of the blade is calculated by rotating sample spectrum which can transform the dynamic process of the rotation of blade into a static process. Thus, the impact of the blade rotation on the subsequent wind vibration reaction of the blade has no need to be included. In this study, a one blade is used to generate the wind velocity. The specific distribution of sampling points is shown in Figure 14. Selecting the sampling point 1 as an example, the fluctuating wind velocity at this point calculated by equation (24) is shown in Figure 15, and the mean wind velocity may be combined with the turbulent wind speed as shown in Figure 16.

5. Blade Load Analysis considering the Blade Rotation

The wind turbines operate primarily by the rotation of blades under external wind loading. The blades are affected by wind loading and gravity load during operation. In the paper, the equation describing the dynamical motion of a lone blade is formulated from Hamilton's principle. The generalized nonconservative force in the presumed degree of freedom is primarily categorised into three components: wind loading element, gravitation element, and damping force. Since the damping in the direction of the assumed degrees of freedom is relatively small, damping force is not considered.

5.1. Calculation of Generalized Wind Loading. In accordance with the blade element theory, any blade can be subdivided into multiple sections with diverse blade elements in order to investigate the force and moments on every blade element. The external power applied on each blade may be acquired through the process of integration in the direction of the blade's wingspan. It is generally assumed that there is no radial airflow between each blade element, i.e., the interaction influence between each blade element is ignored. The lift factor of the blade primarily governs the aerodynamic power. The force exerted by the blades on the airflow is constant compared with the rotor.

In this study, the radius of the impeller is L. v_∞ is the incoming wind speed. The axial induction coefficient is represented by a. β is the $\tan\varphi = (v_\infty(1-a)/\Omega r(1+a'))$ pitch angle. a' represents the tangential induction coefficient. φ denotes the angle formed by the incoming wind velocity and the blade element of the rotating plane. Therefore, the inflow angle is as follows. $v_\infty(1-a)$

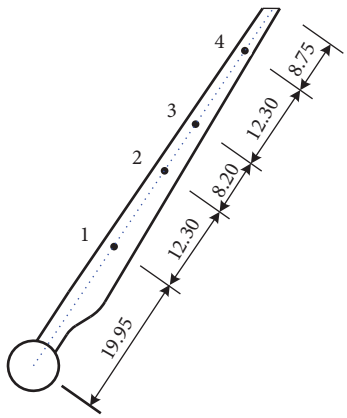

Figure 14: Distribution of sampling points for individual blades.

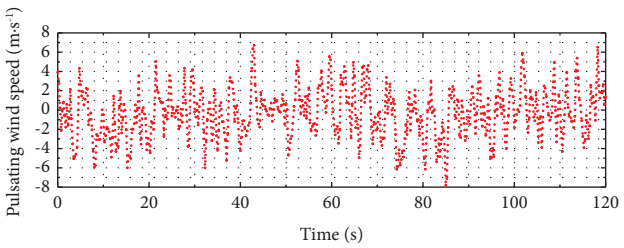

Figure 15: Fluctuating wind speed at P1 on the blade.

represents the functional wind velocity at a length r from the hub, and the induction speed is $\Omega r(1+a')$. $\alpha = \varphi - \theta$ stands for the angle of attack to the blade element airfoil at the local level, c represents the chord length, C_L stands for the lift factor, and C_D stands for the aerodynamic drag factor, as depicted in Figure 17. The airfoil's relative velocity may be represented as follows:

$$V = \sqrt{v_\infty^2 (1-a)^2 + \Omega^2 r^2 \left(1+a'\right)}, \tag{28}$$

where the lift force D and drag force L generated by each blade element's unit length are $D = (1/2)\rho V^2 c C_d$ and $L = (1/2)\rho V^2 c C_l$, respectively.

In general, only the traction force p_T, which runs in parallel with the rotation plane, and the propulsive force p_N which is at a right angle to the rotation plane are taken into account as a rotating blade. As displayed in Figure 18, the lift force and drag force can be broken down across two directions, namely, $p_T = L\sin\phi + D\cos\phi$, $p_N = L\cos\phi + D\sin\phi$, then the towing power on the entire ith blade is $P_{i,\text{in}} = \int_0^L p_{T,i}(x,t)\phi_{\text{in}}(x)\mathrm{d}x$. In accordance with the law of virtual merit, $\delta W = \delta q_{i,\text{in}} P_{i,\text{in}}$ represents the virtual merit performed by the aerodynamic payload across the generalized degree of freedom. Therefore, $Q_{i,\text{in}} = (\delta W/\delta q_{i,\text{in}}) = P_{i,\text{in}}$ represents the generalized aerodynamic load applied to the blade. Axial induction factor a' and tangential induction coefficient are calculated according to the equation.

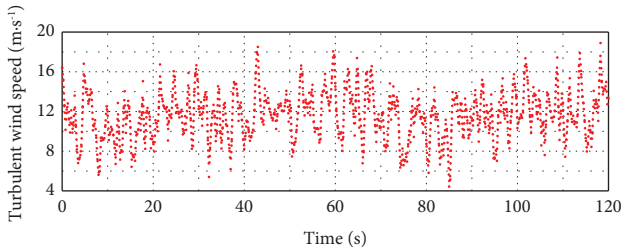

Figure 16: Turbulent wind speed at P1 on the blade.

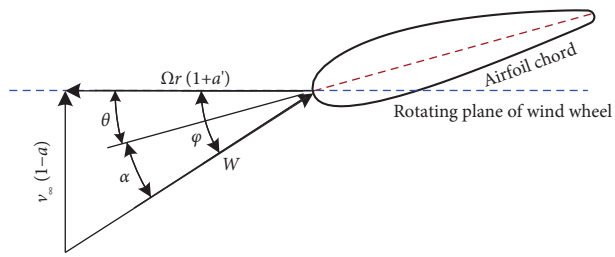

Figure 17: Speed diagram of blade airfoil profile.

$$a = \frac{1}{\left[4\sin^2\phi/(\sigma C_n)+1\right]},$$
$$a' = \frac{1}{\left[4\sin\phi\cos\phi/(\sigma C_t)-1\right]}, \tag{29}$$

where $C_n = C_l\cos\phi + C_d\sin\phi$, $C_t = C_l\sin\phi - C_d\cos\phi$, $\sigma = (cB/2\pi r)$ means the chord length of blade element and B stands for the count of blades.

To gain more accurate calculation results, there is a need to correct various inductions. First of all, the blade element momentum (BEM) theory used here is founded on the supposition that the blade is infinite, but the actual blade has a finite length. In order to make the BEM theory meet the actual situation, the Prandtl tip hub loss factor F is proposed, i.e., $F = 4/\pi^2\cos^{-1}\left(e^{(B(R-r)/2r\sin\phi)}\right)\cdot\cos^{-1}\left(e^{(B(r-R_{\text{hub}})/2R_{\text{hub}}\sin\phi)}\right)$, where r_{hub} is the radius at the hub. Considering the Prandtl tip hub loss factor, the axial induction factor a and tangential induction coefficient a' are expressed as

$$a = \frac{1}{\left[4F\sin^2\phi/(\sigma C_n)+1\right]}, \tag{30}$$

$$a' = \frac{1}{\left[4F\sin\phi\cos\phi/(\sigma C_t)-1\right]}. \tag{31}$$

Secondly, when Prandtl tip hub loss factor [42] is corrected and axial induction factor $a > 0.4$, momentum theory no longer applies in calculation. Hence, the Spera loss factor is proposed to be corrected; that is, axial induction factor a of the blade can be expressed as

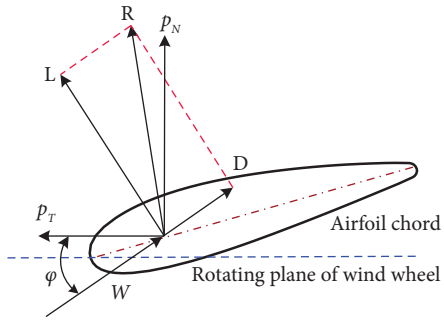

Figure 18: Aerodynamic decomposition diagram of the airfoil surface of the blade element.

$$a = \begin{cases} \dfrac{1}{\left[4F\sin^2\phi/(\sigma C_n)+1\right]}, & a \le 0.4, \\ \dfrac{1}{2}\left\{2+K(1-2a_c) - \sqrt{\left[K(1-2a_c)+2\right]^2+4\left(\mathrm{Ka}_c^2-1\right)}\right\}, & a > 0.4, \end{cases} \tag{32}$$

where $K = (4F\sin^2\phi/\sigma C_n)$.

Combined with equations (30)–(32), the axial induction coefficient, as well as the tangential induction factor of the blade element at P1 under turbulent wind velocity, is progressively acquired through the utilization of the blade element momentum theory, as displayed in Figure 19. Then, the wind load applied on the blade element at P1 along the in-plane and out-of-plane directions can be obtained, as displayed in Figure 20. The blades may experience wind load in a generalized manner from all directions by integrating along the length, as displayed in Figure 21.

5.2. Generalized Gravity Load. The gravitation exerted on the blade is decomposed along the blade's axial and tangential orientations.

$$\begin{cases} \mathrm{d}G_N = m(x)\mathrm{d}x \cdot g\sin\psi_i, \\ \mathrm{d}G_T = m(x)\mathrm{d}x \cdot g\cos\psi_i. \end{cases} \tag{33}$$

In accordance with the law of virtual merit, the work performed by gravitation in the virtual displacement along the generalized degree of freedom is equal to $\delta W_g = \int_0^L m(x)g\sin\psi_i\delta q_{i,\mathrm{in}}\phi(x)\mathrm{d}x$, and then according to equation (33), the generalized gravitational force applied to the blade is

$$\begin{aligned} Q_{i,g} &= \frac{\delta W_g}{\delta q_{i,\mathrm{in}}} \\ &= \int_0^L m(x)g\sin\psi_i\phi(x)\mathrm{d}x. \end{aligned} \tag{34}$$

The generalized gravitation power obtained is displayed in Figure 22.

Assuming that the damping stress is proportional to the damping strain velocity, then the stress-strain relationship could be expressed as, $\sigma = \mathrm{E}c\dot{\varepsilon}$, in which c is the damping coefficient and E stands for the elastic modulus. For the wind turbine structure in this article, the resistance coefficient of each blade can be expressed as $c_b = 2m_b\omega_b\xi_b$ and the drag factor of the tower stands for $c_n = 2m_n\omega_n\xi_n$. The virtual displacement induced by damping force is $W_I = c_b\dot{q}_{i,\mathrm{in}}\int_0^L \mathrm{EI}(x)\varphi_{\mathrm{in}}''(x)^2\mathrm{d}x\delta\dot{q}_{i,\mathrm{in}}$, so the generalized damping force is

$$Q_{\mathrm{in},b} = -c_b\dot{q}_{i,\mathrm{in}}\int_0^L \mathrm{EI}(x)\varphi_{\mathrm{in}}''(x)^2\mathrm{d}x. \tag{35}$$

6. Analysis of Factors Affecting Blade Damping Performance

The vibration reduction system is built into the back-shaped frame between the blade's web and the main girder. The peak value and standard deviation of the reaction are used as the evaluation indices. The ratio of the frequency of the vibration damping system and the modal blade is set to 1.0 to explore the law of the mass ratio, damping ratio, and installation position of the device on the vibration damping efficiency of the blade's tip displacement.

6.1. Influence of Different Parameter Values on Blade Vibration Reduction Performance

6.1.1. Effects of Installation Location and Mass Ratio. Assuming that the damping ratio is $\xi = 50\%$, the influence law of installation position x_0/L and mass ratio μ on the vibration attenuation effectiveness of blade tip displacement is explored. Figure 23 reveals the influence trends of mass ratio and installation position on vibration reduction ratio. It is shown that when the mass ratio reaches in the range of 0.001~0.01, the vibration damping ratio of peak displacement and standard deviation increase having the increase of installation position. When the mass ratio falls within the interval from 0.05~0.10, the vibration reduction ratio of peak displacement as well as standard deviation rises first and then falls as the increase of installation position. When the mass ratio is adjusted to be 0.03, the vibration reduction ratio of peak displacement as well as standard deviation increases first and then decreases at a gentle stage with the increase of installation position. It is worth noting that the TMD is installed at 0.5, an inflection point occurs in the curve with a large mass ratio. That is because blades made of lightweight and high-strength materials are variable-section cantilever rotating structures, and their stiffness decreases as the size of the blades grows, which will cause the blades to be affected by the whipping effect. This leads to an inflection point in the curve, which means that the damping ratio suddenly decreases. When the TMD having a large mass ratio is installed closer to the blade tip, it is challenging for the TMD to adjust the vibration frequency to the height frequency of the tip due to the limitation of the blade space, which leads to poor vibration damping effect for large mass

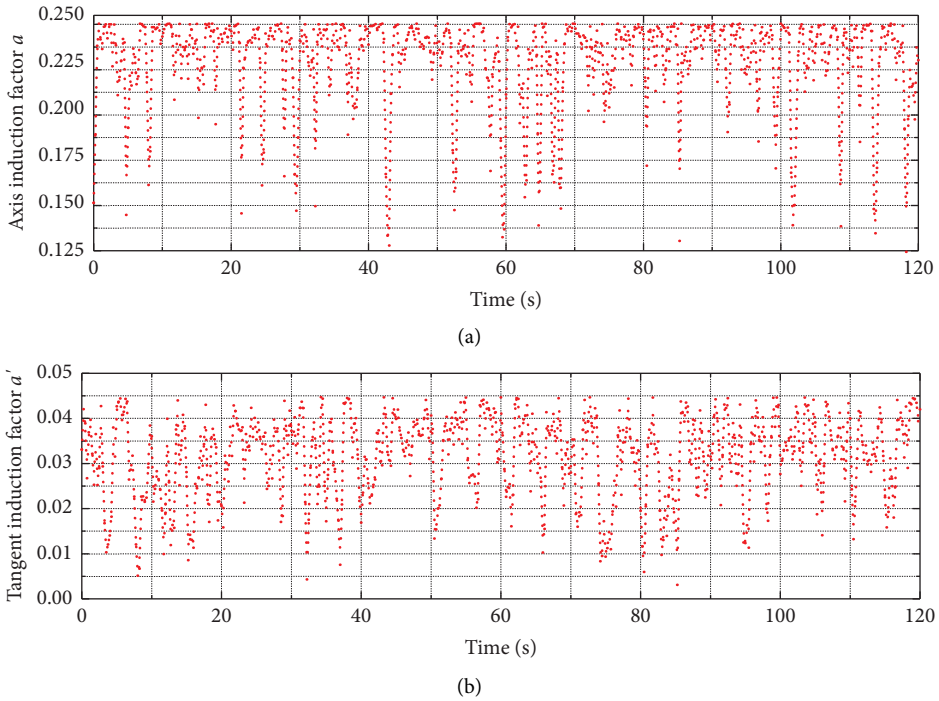

Figure 19: Blade element induction factor at P1 of the blade. (a) Axial induction factor of blade element at P1. (b) Axial induction factor of blade element at P1.

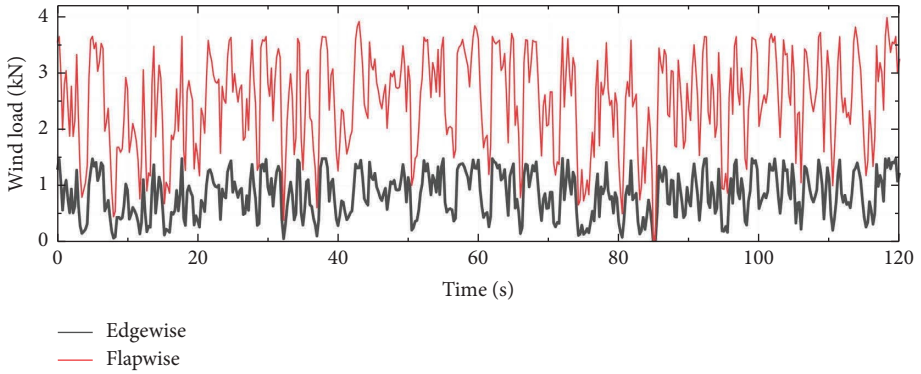

Figure 20: Loads on each direction of blade element at P1.

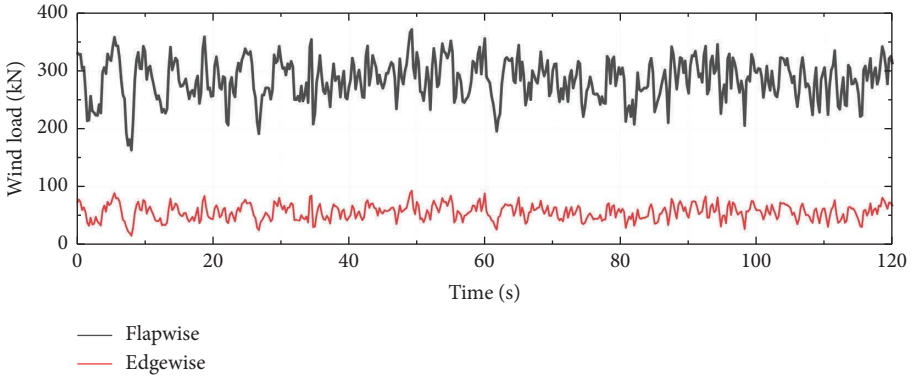

Figure 21: The blade is subjected to wind loadings in all directions.

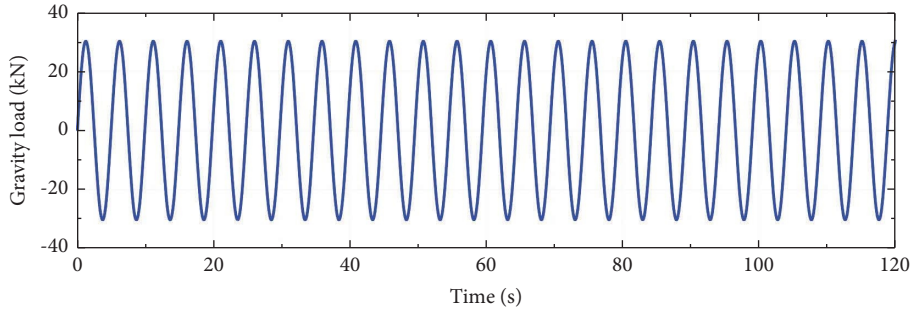

FIGURE 22: Generalized gravitational load on the blade.

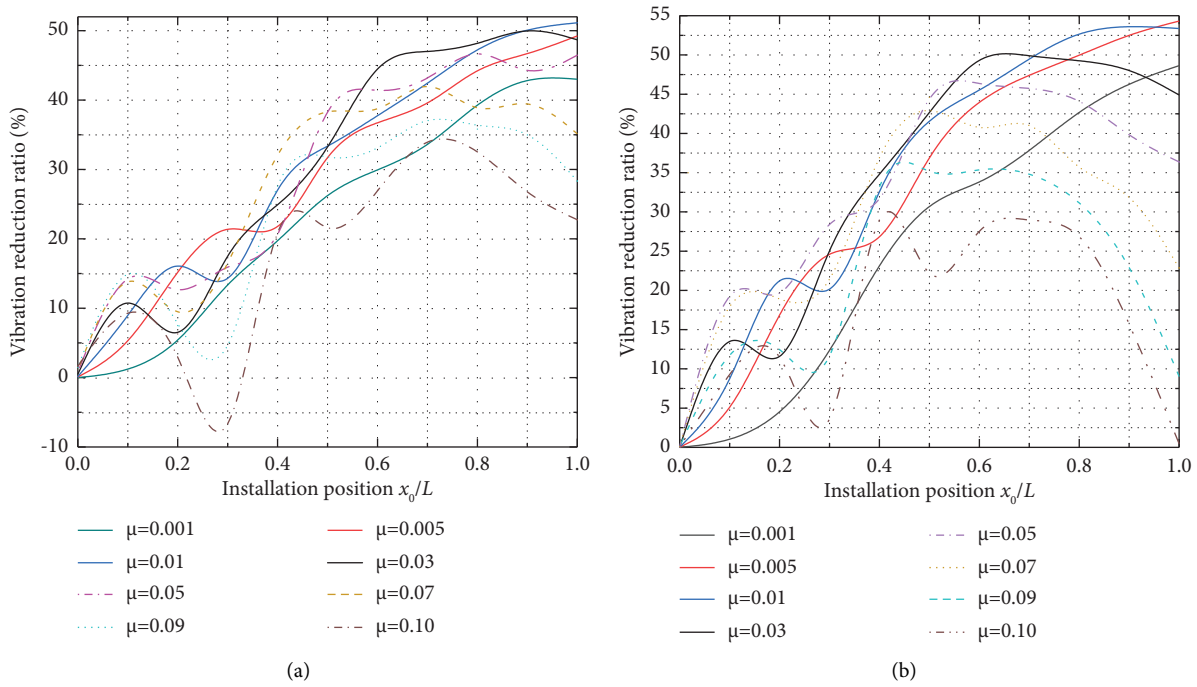

FIGURE 23: Influence of mass ratio and installation position on the vibration reduction ratio. (a) Vibration reduction ratio of peak displacement. (b) Vibration reduction ratio of the standard deviation of displacement.

ratio. In the whole analysis process, when the mass ratio is between 0.01 and 0.03, the change level of the vibration damping ratio is relatively flat. The closer the blade tip, the higher the vibration damping ratio is relatively.

The vibration damping ratio of blade tip displacement of blades changes continuously with the value of mass ratio and installation position. When the vibration control device is designed, the maximum vibration reduction ratio is achieved with no loss of aerodynamic performance. Figure 24 shows the distribution range of the maximum vibration reduction ratio. The figure shows that when the mass ratio is about 0.01 and the installation position is in the range of 0.8~1.0, the vibration damping ratio of the standard deviation of displacement may be up to 53.07%. When the mass ratio falls within the interval from 0.01 to 0.03 and the installation position is between 0.9 and 1.0, the peak vibration damping ratio of displacement can reach 49.73%. Therefore, when the damping ratio is selected as 50%, only considering the vibration damping ratio of blade tip displacement, the optimal mass ratio of the vibration suppression control device is 0.01 and the optimal installation position is around 0.9~1.0.

6.1.2. Effects of Mass Ratio and Damping Ratio. When the damping ratio is 50%, the relationship between the installation position x_0/L and the mass ratio μ is investigated. The relative parameter value of the mass ratio taken as 0.03 and the installation position taken as 0.84 is better. However, the optimal damping ratio of the vibration control design is not 50%. Therefore, when the installation position is 0.84, the correlation between the mass ratio and the damping ratio is explored.

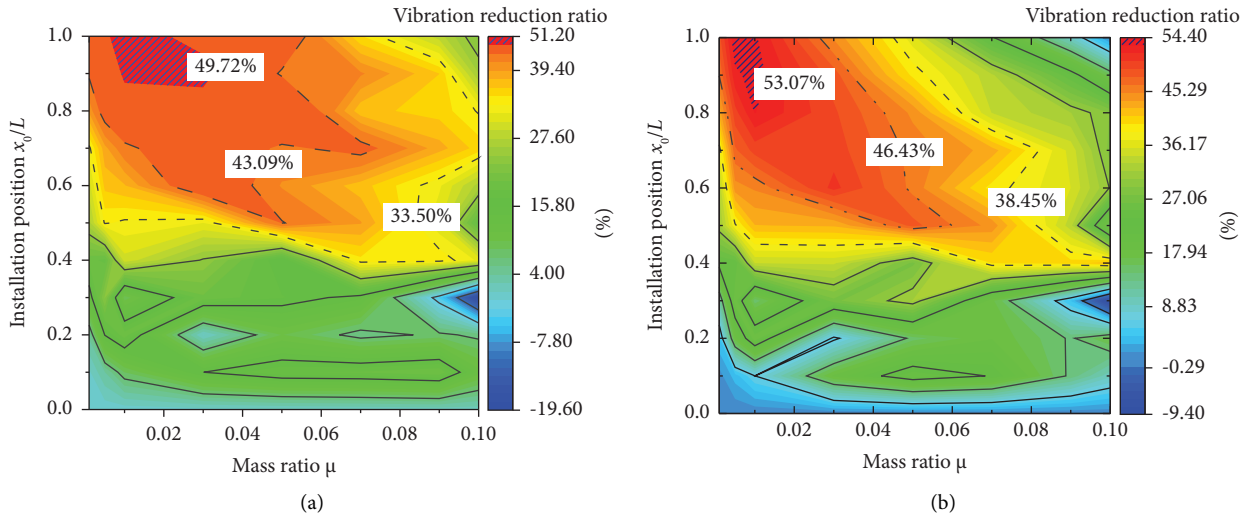

Figure 24: Distribution of maximum vibration reduction ratio under effects of installation location and mass ratio.

Figure 25 describes the impact of mass ratio and installation on the vibration reduction rate. The figure indicates that the vibration suppression ratio of the peak and standard deviation of the displacement first show an increment of about 20%, then remain flat with the increase of the damping ratio, and finally, the vibration damping ratio reaches the maximum when the damping ratio is about 20%. If the damping ratio is 20%, the vibration damping ratio of standard deviation and peak displacement increase first and then fall as the mass ratio increases.

Figure 26 shows the distribution range of the maximum damping ratio. The figure shows that when the damping ratio ranges from 15% to 40%, the vibration damping ratio of the standard deviation at blade's tip displacement is 53.84%. When the mass ratio is close to 0.01, the vibration damping rate of peak displacement at the blade's tip is 49.92% when the mass ratio varies from 0.01 to 0.03. Therefore, it could be viewed from Figure 23, for the vibration suppression ratio of the tip displacement, the optimal mass ratio of the damping system is 0.01 and the optimal damping ratio range is 15%~40% when the installation position is selected as 0.84.

6.1.3. Impact of Damping Ratio and Installation Location. Based on the principle of the minimum mass ratio and making full use of the movement of the mass block running on the inside wall of the web, the mass ratio is assumed to be 0.02. From the analysis results in Figure 27, the correlation between the damping ratio and the installation position is analyzed. Figure 28 reveals the trend of the vibration suppression ratio with the damping ratio and installation position. It could be known from Figure 28 that the vibration damping ratio of standard deviation and peak displacement at blade's tip increase gradually with the installation position closer to the blade tip for a certain damping ratio. When the installation position x_0/L is taken between 0.75 and 1.0, the changing trend of the damping ratio is relatively slow and maintains a relatively stable level. At the same time, for any fixed installation position, the vibration damping ratio of standard deviation and peak displacement rises first and then falls as the damping ratio grows. In the whole process, when the damping ratio is 20%, the variation of damping ratio with the value of installation position is relatively flat. When the installation position x_0/L is taken between 0.75 and 1.0, the vibration reduction ratio is relatively higher under each damping ratio.

Figure 27 shows the changing law of the damping ratio with the installation position and damping ratio. As seen in Figure 27, when the installation position x_0/L of the vibration damping system is taken between 0.6 and 1.0, the vibration damping efficiency of standard deviation and peak value of the blade tip will reach more than 40.06%, and the effect on the vibration damping rate is relatively small as the damping ratio rises. When the installation position is defined as 0.6 and the damping ratio ξ is set between 15% and 20%, the vibration damping efficiency at the blade tip reaches 52.09%. Therefore, if the mass ratio becomes 0.02, the optimal parameter value to make the damping ratio maximum is as follows: the damping ratio is 20%, and the installation position is 0.60.

6.2. Parameter Optimization. Figure 29 shows the variation pattern of peak displacement for the mass block. It could be clearly illustrated from the figure that on the condition of the parameters $\mu = 0.01$, $\xi = 50\%$, and $x_0/L > 0.68$, the mass block touches inside wall of the blade web when the vibration control device works, which cannot meet the design requirements. When the installation position is adjusted to 0.84 and the mass ratio exceeds 0.01, the mass block contacts just with the inside wall of the web in the operation. If the mass ratio is 0.03, the tendency of displacement about the mass block is relatively flat. While when the damping ratio is set to 50%, in order to guarantee that the mass block avoids contact with the inside wall of the web with the highest vibration damping efficiency at blade tip displacement, the

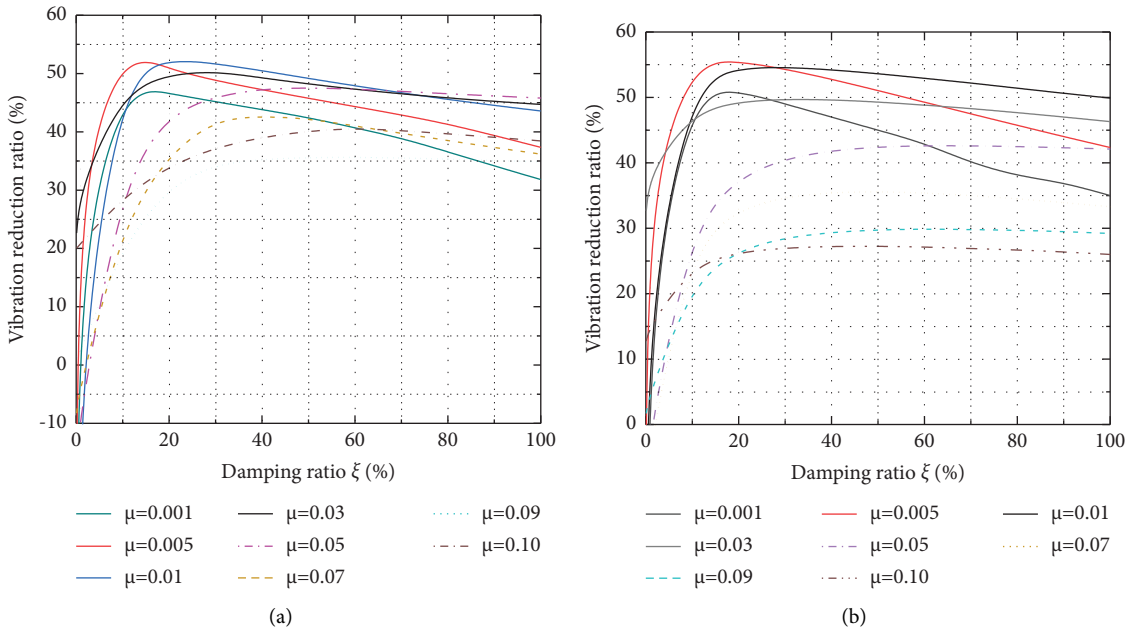

Figure 25: Effect of mass ratio and installation position on the vibration reduction ratio. (a) Vibration reduction ratio of the peak displacement. (b) Vibration reduction ratio of the standard deviation of displacement.

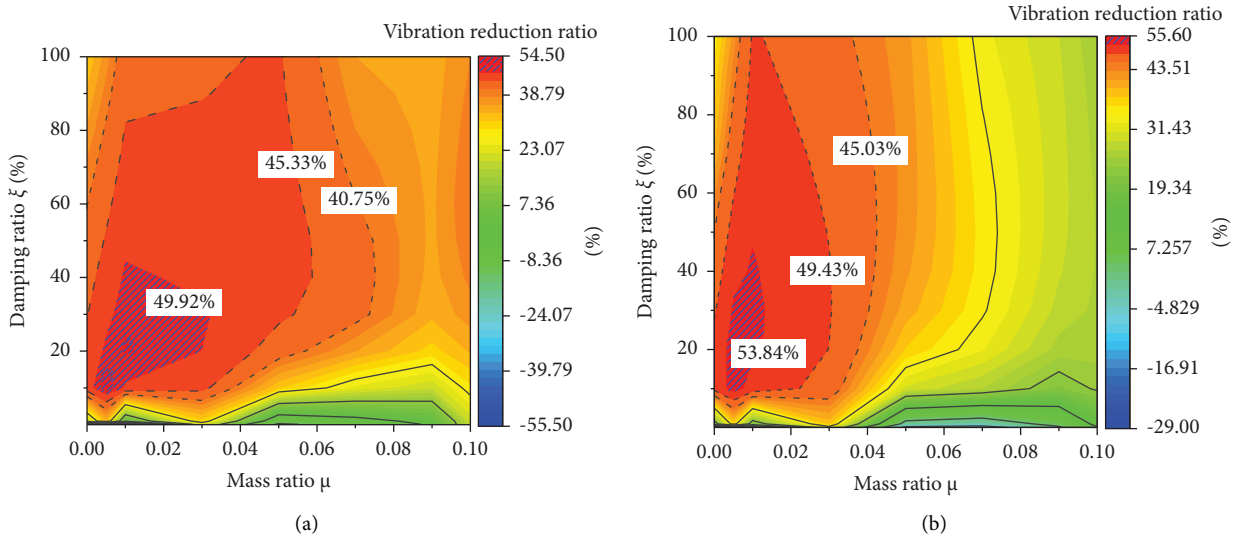

Figure 26: Distribution of maximum vibration reduction ratio under effects of mass ratio and damping ratio.

mass ratio μ could be set to 0.03 and the installation position x_0/L should be set to 0.84 in combination with Figure 24.

Figure 30 describes the variation pattern of peak displacement for the mass block as the mass ratio and damping ratio are varied. As shown in Figure 30, when the installation position is 0.84, the effective chord length of the relevant airfoil is constant, and the displacement of the mass block decreases as the mass ratio increases. If the mass ratio is above 0.02, the change law is relatively flat. In order to guarantee that the mass block avoids contact with the inside wall of the web in the operation process, in this analysis process, the mass ratio is not less than 0.02 and the damping ratio is greater than 50%, which can meet the design requirements.

For different parameter values, the displacement of mass blocks is different. Figure 31 shows the pattern of displacement variation for the mass block changed with damping ratio and installation position. From the figure, the installation position is nearer to the blade's tip, and the displacement of the mass block is increased. By increasing the damping ratio, the displacement of the mass block falls gradually and the decrease values of each displacement decrease gradually. About the collision between the vibration control device and the inside wall of the web of the wind

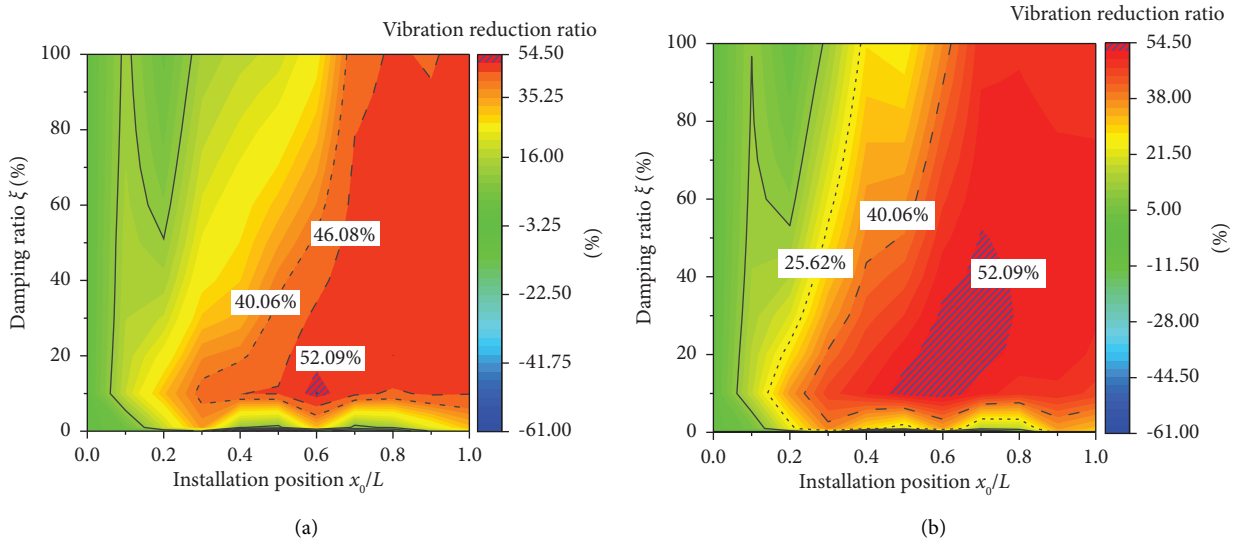

Figure 27: Distribution of maximum vibration reduction ratio under damping ratio and installation location.

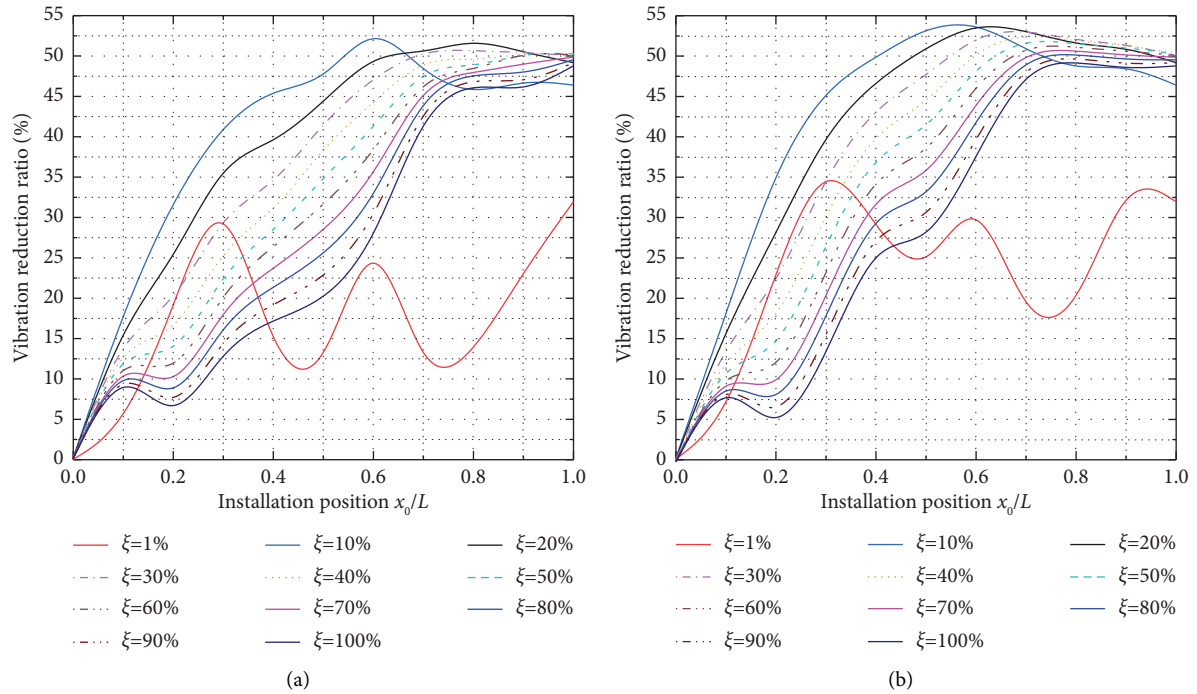

Figure 28: Influence of damping ratio and installation position on vibration reduction ratio. (a) Vibration reduction ratio of peak displacement. (b) Vibration reduction ratio of the standard deviation of displacement.

turbine, it can be found that when the damping ratio is set to 20% and the installation position of the vibration damping system is set as 0.65, as well as the peak displacement of the mass block in the operational process just touches with the inside wall of the web. Therefore, if the damping ratio is set as 20% and the installation position is set as 0.60 in the whole analysis process, there is no collision between the vibration control device during operation and the inside wall of the blade web, which satisfies the design demands.

6.3. Analysis of Vibration Absorption Performance under Optimal Parameters. The vibration control of the blade in the in-plane direction is carried out by a damping control device having a damping ratio of 20%, a mass ratio of 0.02, and an installation position of 0.60. Figure 32 reveals the displacement-time of the blade tip. Based on the data, the peak displacement at the blade tip reaches 2.46 m and the standard deviation reaches 0.81 for the without controlling the case. For the controlled case, the peak displacement of

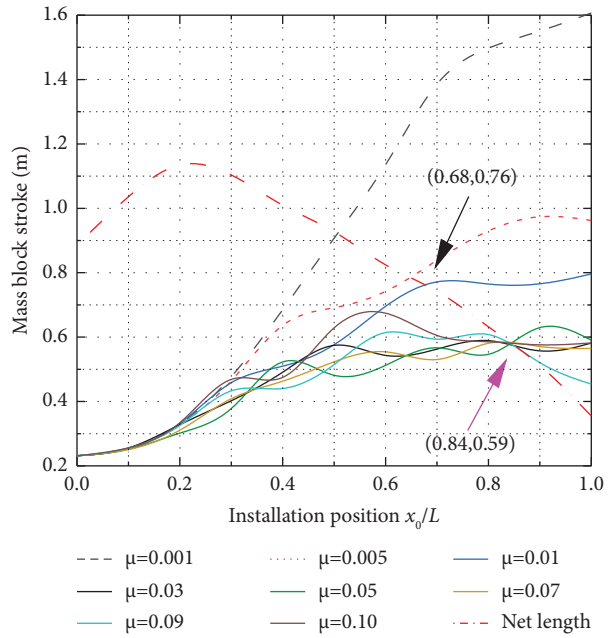

Figure 29: Law of variation of the peak displacement of the mass block under effects of installation location and mass ratio.

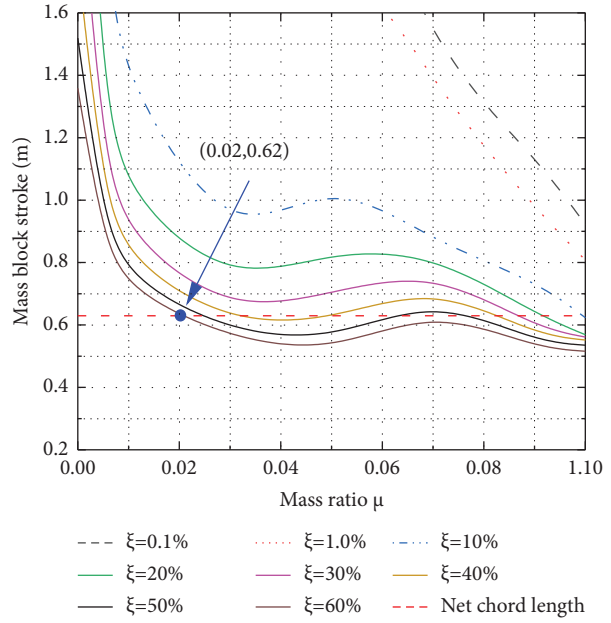

Figure 30: Law of variation of the peak displacement of the mass ratio.

the blade tip is 1.22 m and the standard deviation reaches 0.36. In comparison with the uncontrolled condition, the peak displacement at the blade's tip experiences a reduction of 50.34% and the standard deviation experiences a reduction of 54.18% under the controlled condition.

Figure 33 displays the time history of the base bending moment about the blade. It could be noted that the displacement at the blade's tip is reduced and the blade root bending moment is also effectively reduced during the period when the blade experiences elastic strain, which can avoid damage of the blade root. Based on the investigation of standard and peak values as the control criteria, the passive vibration damping device installed in the wind turbine blade has a positive effect on regulating the displacement at the blade tip.

The TMD-based vibration reduction control device, which is installed on the inside wall of the blade web, aims to fully utilize the internal space of the blade during operation

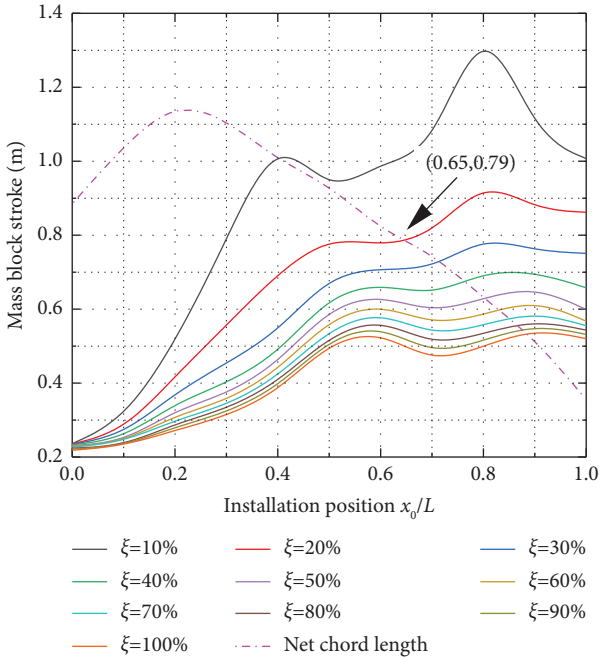

Figure 31: Law of variation of the peak displacement of the mass block under effects of damping ratio and installation location.

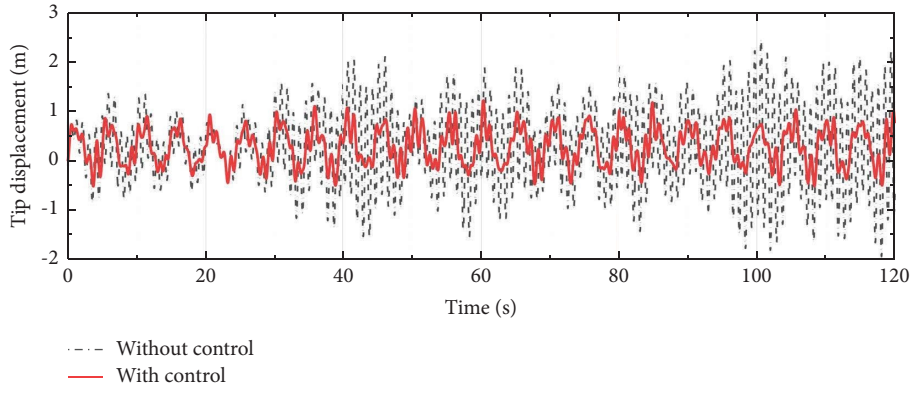

Figure 32: Time history of blade tip displacement.

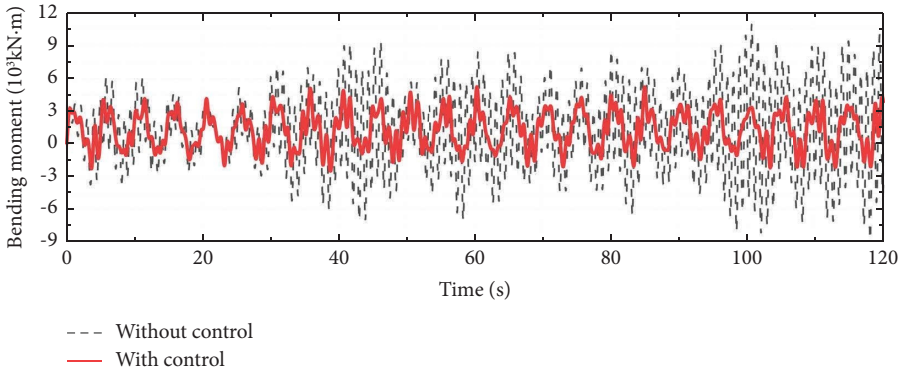

Figure 33: Time history of blade root bending moment.

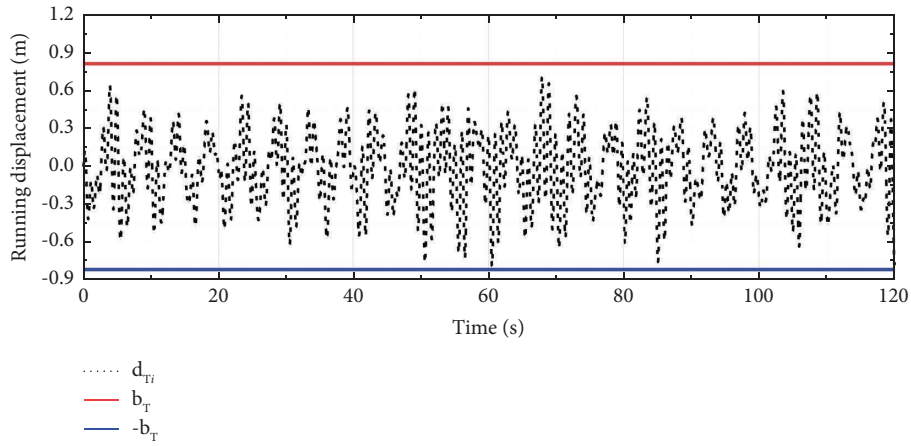

Figure 34: Time history of mass block movement.

to avoid pounding. The displacement of the mass block is shown in Figure 34. The peak value of the operating movement of the mass block is 0.79 m, while the chord length of the radial position of the inside wall of the blade web is 3.26 m. After installing the vibration control device, the chord length for its operation is the net chord length, which is 0.84 m. Therefore, when the optimal parameter value is selected, the displacement of the mass block is not as much as the net chord length set above, which meets the requirements of vibration reduction analysis.

7. Conclusions

In this study, a TMD-based device is designed for vibration damping of the blade in the in-plane direction in the rotating state. Under the condition of resonance, the effect law of the parameters including mass ratio, damping ratio, and installation position of the device on the vibration suppression performance of tip displacement is investigated, and the following conclusions are obtained:

(1) By comparing the Von–Karman spectrum having the rotating sample spectrum obtained using the Von–Karman spectrum as the source spectrum, it can be found that the energy distribution of the rotating sample spectrum in the high-frequency part is obviously different from that of the Von–Karman spectrum.

(2) The parameters, e.g., the mass ratio μ, damping ratio ξ, and installation position x_0/L, show a strong improvement on the vibration damping performance of the blade tip displacement. As the mass ratio rises, that effectiveness first increases and then decreases. Meanwhile, as the installation position is closer to the blade tip, the vibration reduction ratio first increases and then gradually flattens. In addition, as the damping ratio increases, the vibration decreasing ratio first rises rapidly and then decreases gently.

(3) The operation displacement of the mass block decreases first and then remains stable as mass ratio increases and decreases as the damping ratio increases. In the meantime, the displacement increases when the installation position approaches the blade's tip. The mass ratio should be minimised so as to ensure satisfactory performance of the vibration reduction control device and to prevent colliding phenomena between the mass block and the inside wall of the blade web during run time, and the installation position should be as far away as possible from the blade's tip while increasing the damping ratio.

(4) Using the optimal parameter values, the vibration reduction control device designed in this paper could be effective in suppressing the peak displacement of the tip and the bending moment at the blade root under the condition of ensuring mass block against colliding with the inside wall of the blade's web. If the relative optimal settings of mass ratio $\mu = 0.03$, damping ratio $\xi = 15\%$, and installation position $x_0/L = 0.55$, the largest peak vibration damping ratio of blade tip attains 52.28%, and the maximum standard vibration damping ratio attains 53.75%. In addition, the smallest gap between the lateral movement of the mass block and web is 0.02 m when the device is at operation, which meets the conditions for the operation of the device. In addition, the minimum distance between the horizontal displacement of mass block and web is 0.02 m when the device is at operation, which meets the conditions for the operation of the device.

Data Availability

The data that support the findings of this study are available from the corresponding author upon request.

Disclosure

Wanrun Li present address is Institute of Earthquake Protection and Disaster Mitigation, Lanzhou University of Technology, 287 Langongping Rd, Qilihe District, Lanzhou 730050, China.

Conflicts of Interest

The authors declare that there are no conflicts of interest.

Authors' Contributions

Wanrun Li conceptualized the study, designed the methodology, supervised the study, provided the resources, wrote, reviewed, provided guidance, administered the project, and acquired the funding. Shuanbao Yan conceptualized the study, curated the data, conducted the analysis, prepared the original draft of the manuscript, and wrote the manuscript. Ganggang Li conceptualized the study, designed the methodology, prepared the program, validated the data, and designed the device. Yongfeng Du conceptualized the study, designed the methodology, and provided guidance.

Acknowledgments

The authors gratefully acknowledge the financial support from the Gansu Province Science Fund for Distinguished Young Scholars (grant no. 21JR7RA267) and the National Natural Science Foundation of China (grant nos. 51568041 and 52068049).

References

[1] R. Li, X. Wang, and Q. Wang, "Doesrenewable energy reduce ecological footprint atthe expense of economic growth? An empirical analysis of 120 countries," *Journal of Cleaner Production*, vol. 346, Article ID 131207, 2022.

[2] R. Akram, F. Chen, F. Khalid, Z. Ye, and M. Majeed, "Heterogeneous effects of energy efficiency and renewable energy on carbon emissions: evidence from developing countries," *Journal of Cleaner Production*, vol. 247, Article ID 119122, 2020.

[3] S. Yao, M. Chetan, D. Griffith et al., "Aero-structural design and optimization of 50 MW wind turbine with over 250-m blades," *Wind Engineering*, vol. 46, no. 1, pp. 273–295, 2022.

[4] S. Sarkar and B. Fitzgerald, "Fluid inerter for optimal vibration control offloating offshore wind turbine towers," *Engineering Structures*, vol. 266, Article ID 114558, 2022.

[5] M. Hansen, "Aeroelastic instability problems for wind turbines," *Wind Energy*, vol. 10, no. 6, pp. 551–577, 2007.

[6] Z. Zhang, J. Li, S. Nielsen, and B. Basu, "Mitigation of edgewise vibrations in wind turbine blades by means of roller dampers," *Journal of Sound and Vibration*, vol. 333, no. 21, pp. 5283–5298, 2014.

[7] S. Das, M. Sajeer, and A. Chakraborty, "Vibration control of horizontal axis offshore wind turbine blade using SMA stiffener," *Smart Materials and Structures*, vol. 28, no. 9, Article ID 095025, 2019.

[8] K. Thomsen, J. Petersen, E. Nim, S. Øye, and B. Petersen, "A method for determination of damping for edgewise blade vibrations," *Wind Energy*, vol. 3, no. 4, pp. 233–246, 2000.

[9] A. Ahlstrøm, "Influence of wind turbine flexibility on loads and power production," *Wind Energy*, vol. 9, no. 3, pp. 237–249, 2016.

[10] Z. Zhang, "Optimal tuning of the tuned mass damper (TMD) for rotating wind turbine blades," *Engineering Structures*, vol. 207, no. 3, Article ID 110209, 2020.

[11] B. Fitzgerald, A. Staino, and B. Basu, "Wavelet-based individual blade pitch control for vibration control of wind turbine blades," *Structural Control and Health Monitoring*, vol. 26, no. 1, Article ID e2284, 2019.

[12] C. Jia, L. Wang, E. Meng et al., "Combining LIDAR and LADRC for intelligent pitch control of wind turbines," *Renewable Energy*, vol. 169, pp. 1091–1105, 2021.

[13] X. Yin, Y. Lin, W. Li, and Y. Gu, "Integrated pitch control for wind turbine based on a novel pitch control system," *Journal of Renewable and Sustainable Energy*, vol. 6, no. 4, Article ID 043106, 2014.

[14] E. Bossanyi, "Further load reductions with individual pitch control," *Wind Energy*, vol. 8, no. 4, pp. 481–485, 2005.

[15] E. Bossanyi, "Individual blade pitch control for load reduction," *Wind Energy*, vol. 6, no. 2, pp. 119–128, 2003.

[16] A. Tabrizikahou, M. Kuczma, P. Nowotarski, M. Kwiatek, and A. Javanmardi, "Sustainability of civil structures through the application of smart materials: a review," *Materials*, vol. 14, no. 17, p. 4824, 2021.

[17] L. Zhao, M. Yu, J. Fu, M. Zhu, and B. Li, "A miniature MRE isolator for lateral vibration suppression of bridge monitoring equipment: design and verification," *Smart Materials and Structures*, vol. 26, no. 4, Article ID 047001, 2017.

[18] X. Lu, Q. Zhang, D. Weng et al., "Improving performance of a super tall building using a new eddy-current tuned mass damper," *Structural Control and Health Monitoring*, vol. 24, no. 3, Article ID e1882, 2017.

[19] K. Kwok and B. Samali, "Performance of tuned mass dampers under wind loads," *Engineering Structures*, vol. 17, no. 9, pp. 655–667, 1995.

[20] Y. Yang and C. Li, "Performance of tuned tandem mass dampers for structures under the ground acceleration," *Structural Control and Health Monitoring*, vol. 24, no. 10, Article ID e1974, 2017.

[21] R. Greco, A. Lucchini, and G. Marano, "Robust design of tuned mass dampers installed on multi-degree-of-freedom structures subjected to seismic action," *Engineering Optimization*, vol. 47, no. 8, pp. 1009–1030, 2015.

[22] B. Fitzgerald, B. Basu, and S. Nielsen, "Active tuned mass dampers for control of in-plane vibrations of wind turbine blades," *Structural Control and Health Monitoring*, vol. 20, no. 12, pp. 1377–1396, 2013.

[23] B. Fitzgerald and B. Basu, "Cable connected active tuned mass dampers for control of in-plane vibrations of wind turbine blades," *Journal of Sound and Vibration*, vol. 333, no. 23, pp. 5980–6004, 2014.

[24] C. Cong, "Decentralized control of vibrations in wind turbines using multiple active tuned mass dampers with stroke constraint," *Advances in Mechanical Engineering*, vol. 10, no. 12, Article ID 168781401881675, 2018.

[25] P. Murtagh, A. Ghosh, B. Basu, and B. Broderick, "Passive control of wind turbine vibrations including blade/tower interaction and rotationally sampled turbulence," *Wind Energy*, vol. 11, no. 4, pp. 305–317, 2008.

[26] V. Dinh and B. Basu, "Passive control of floating offshore wind turbine nacelle and spar vibrations by multiple tuned mass dampers," *Structural Control and Health Monitoring*, vol. 22, no. 1, pp. 152–176, 2015.

[27] Z. Zhang, B. Basu, and S. Nielsen, "Tuned liquid column dampers for mitigation of edgewise vibrations in rotating wind turbine blades," *Structural Control and Health Monitoring*, vol. 22, no. 3, pp. 500–517, 2015.

[28] B. Basu, Z. Zhang, and S. Nielsen, "Damping of edgewise vibration in wind turbine blades by means of circular liquid dampers," *Wind Energy*, vol. 19, no. 2, pp. 213–226, 2016.
[29] Z. Zhang, S. Nielsen, B. Basu, and J. Li, "Nonlinear modeling of tuned liquid dampers (TLDs) in rotating wind turbine blades for damping edgewise vibrations," *Journal of Fluids and Structures*, vol. 59, pp. 252–269, 2015.
[30] Z. Zhang and T. Larsen, "Optimal calibration of the rotational inertia double tuned mass damper (RIDTMD) for rotating wind turbine blades," *Journal of Sound and Vibration*, vol. 493, Article ID 115827, 2021.
[31] Y. Qiao, J. Han, C. Zhang, J. Chen, and K. Yi, "Finite element analysis and vibration suppression control of smart wind turbine blade," *Applied Composite Materials*, vol. 19, no. 3-4, pp. 747–754, 2012.
[32] F. Bolat and S. Sivrioglu, "Active vibration suppression of elastic blade structure: using a novel magnetorheological layer patch," *Journal of Intelligent Material Systems and Structures*, vol. 29, no. 19, pp. 3792–3803, 2018.
[33] S. Sivrioglu, F. Bolat, and E. Erturk, "Active vibration control of a blade element with uncertainty modeling in PZT actuator force," *Journal of Vibration and Control*, vol. 25, no. 21-22, pp. 2721–2732, 2019.
[34] A. Staino, B. Basu, and S. Nielsen, "Actuator control of edgewise vibrations in wind turbine blades," *Journal of Sound and Vibration*, vol. 331, no. 6, pp. 1233–1256, 2012.
[35] C. Cong, "Stochastic vibrations control of wind turbine blades based on wirelesssensor," *Wireless Personal Communications*, vol. 102, no. 4, pp. 3503–3515, 2018.
[36] H. Jokar, R. Vatankhah, and M. Mahzoon, "Active vibration control of horizontal-axis wind turbine blades using disturbance observer-based boundary control approach," *Engineering Structures*, vol. 275, Article ID 115323, 2023.
[37] B. Chen, Z. Zhang, X. Hua, S. Nielsen, and B. Basu, "Enhancement of flutter stability in wind turbines with a new type of passive damper of torsional rotation of blades," *Journal of Wind Engineering and Industrial Aerodynamics*, vol. 173, pp. 171–179, 2018.
[38] W. Sarwar and R. Sarwar, "Vibration control devices for building structures and installation approach: a review," *Civil and Environmental Engineering Reports*, vol. 29, no. 2, pp. 74–100, 2019.
[39] J. Wang, C. Lin, and B. Chen, "Vibration suppression for high-speed railway bridges using tuned mass dampers," *International Journal of Solids and Structures*, vol. 40, no. 2, pp. 465–491, 2003.
[40] T. Soni, A. Das, and J. Dutt, "Active vibration control of ship mounted flexible rotor-shaft-bearing system during seakeeping," *Journal of Sound and Vibration*, vol. 467, Article ID 115046, 2020.
[41] Z. Zhang, S. Nielsen, F. Blaabjerg, and D. Zhou, "Dynamics and control of lateral tower vibrations in offshore wind turbines by means of active generator torque," *Energies*, vol. 7, no. 11, pp. 7746–7772, 2014.
[42] H. Mol, *Aerodynamics of Wind Turbines*, Science Publishers Ltd, London, UK, 2000.